Moisture Swing Direct Air Capture for Carbon Dioxide Enrichment in Closed Greenhouse Environments

MSc Thesis Report

J.J.P. Vianen

Delft University of Technology
Tuesday, June 25, 2024

Moisture Swing Direct Air Capture for Carbon Dioxide Enrichment in Closed Greenhouse Environments

MSc Thesis Report

by

J.J.P. Vianen

A thesis presented to obtain the degree of Master of Science in Mechanical Engineering
at the Delft University of Technology,
to be defended publicly on Tuesday June 25, 2024 at 2:00 PM.

Student number:	4690788	
Project duration:	September 4, 2023 – June 18, 2024	
Thesis committee:	Dr. ir. T.M.J. Nijssen,	TU Delft P&E, supervisor
	Prof. dr. ir. T.J.H. Vlugt,	TU Delft P&E
	Prof. dr. ir. T. Keviczky,	TU Delft DCSC

Cover image: Photo by Katrien van Cromburgghe on Unsplash.

This thesis is confidential and cannot be made public until June 25, 2024.

TU Delft

Preface

This master's thesis is written to obtain the degree of Master of Science in Mechanical Engineering with specializations in the track Energy, Flow, and Process Technology at the Delft University of Technology. The research presented herein focuses on the development and analysis of a moisture swing direct air capture system aimed to enhance carbon dioxide concentrations in a closed greenhouse environment, with the goal to boost crop growth in a sustainable and feasible way.

The motivation for this study comes from the increase in global demand for food and the need to use more sustainable solutions instead of fossil fuels. Enhancing the carbon dioxide levels within a greenhouse has been identified as a method to improve crop yields. Currently traditional methods are fossil-fuel based or energy intensive. Using almost only water as the driving force in a system could be very interesting system and this thesis explores the feasibility of this innovative idea.

I would like to thank my supervisor from the university, dr. ir. Tim Nijssen, a lot for his great instructive support throughout this project. His supervision and expertise in direct air capture have assisted me to achieve the best possible findings for this thesis. I ran into a number of problems during this project, which I was able to solve with thanks to Tim's invaluable insights and guidance.

I am also grateful to the the group of faculty employees and students at the Process and Energy Department, with whom we had a group meeting once every two weeks including three progress presentations. The meetings I had the opportunity to present was helpful through the feedback and various questions that led to new insights.

Lastly I want to thank my family for their support not only during this thesis, but during my complete study at the university. I hadn't thought it, but my dad, a horticultural grower, has passed on to me some interest in the horticulture sector.

I hope the insights and findings of the presented work in this thesis will pave the way for future research and practical implementations in the field of greenhouse agriculture, to create a more sustainable way of growing crops.

J.J.P. Vianen Delft, June 2024

Abstract

While CO_2 is one of the factors increasing the global temperature, it is also utilized in the agriculture to enhance crop yield. In the agriculture, a sustainable solution to CO_2 mitigation would potentially lie in the greenhouses. A moisture swing direct air capture system can adsorb CO_2 from the air through changes in humidity levels between the adsorption and the desorption stages. During adsorption dry air is required, while during desorption humid air is required. In a greenhouse, where humid air is typically required for the crops and CO_2 enhancement is often achieved through fossil-fuel combustion, a moisture swing system could be a sustainable innovation.

Insights into the feasibility and potential implementation of a moisture swing column designed to enhance CO_2 concentrations within a greenhouse are obtained through an investigation of the key parameters of the sorbent, the effect of global climate conditions on the sorbent, a parameter sensitivity analysis of the performance of the system, and a preliminary techno-economic viability assessment.

A one-dimensional numerical model was developed to solve the mass balance of a cylindrical adsorption column. Critical key parameters that affect the CO_2 saturation coverage of the sorbent are the gas phase CO_2 concentration, the relative humidity, and the temperature. Investigated is how these conditions vary globally, highlighting optimal arid climate regions with a high saturation coverage. It was found that seasonal and diurnal deviations are significantly higher in regions where a lower saturation coverage can be reached. From the sensitivity analysis of the parameters and conditions, it was that a 1.6-meter-long column achieved a system efficiency of 15.0 micromoles of CO_2 per kilogram sorbent per second, a water loss of 45.4 moles of water per mole of CO_2, and a system productivity of 9.05 moles of CO_2 per second. In the short term, the majority of costs are attributed to the capital expenditures, whereas in the long term, operational expenditures become the dominant expense.

Contents

1 Introduction

Carbon dioxide (CO_2) plays a pivotal role in the climate change, as the rising of the atmospheric CO_2 concentrations negatively impact the climate. However, CO_2 does not only have negative effects, it is also an essential building block for crops and plants. In the agriculture, CO_2 is even used to enhance the crop yield. Greenhouses can potentially be the intersection between the CO_2 mitigation and enhanced crop productivity, which is becoming crucial as the global population continues to rise and sustainable farming becomes more and more important.

So, while CO_2 is often viewed as a pollutant in the atmosphere, it is beneficial in a closed greenhouse environment. Capturing the CO_2 from the air and utilizing it in greenhouses could be a sustainable addition to greenhouses. However, the method of capturing CO_2 must also be sustainable. Traditional methods, like CO_2 generators or natural gas burners with CO_2 as a byproduct of combustion, can be energy-intensive, but there are materials that can absorb CO_2 from dry air and release it in humid air. Shifting towards moisture swing direct air capture (DAC) is particularly intriguing because it reduces the need for substantial energy, with primary cost being the maintenance of water supply to sustain the required humidity levels within the greenhouse. This thesis explores the innovative concept of using such a moisture swing material for DAC to increase the CO_2 levels in a closed greenhouse, studying the efficiency, feasibility, and viability. This investigation is performed through the development and analysis of an one-dimensional numerical model to answer the main research question:

What are the feasibility and efficiency of implementing a moisture-swing DAC system for CO_2 enrichment in a closed greenhouse environment for optimized plant growth and productivity?

To achieve a proper answer for our research and this question above, the following sub-questions must be answered to substantiate a conclusion:

1. What are the key parameters impacting the feasibility and efficiency of the system?
2. How does the moisture swing sorbent perform under various climatic conditions worldwide, considering specific combinations of humidity, and temperature?
3. How do the parameters and conditions affect the performance of the moisture swing DAC system in a closed greenhouse environment?
4. How do water availability and energy costs around different places in the world influence the economic feasibility of moisture swing DAC for CO_2 enrichment in greenhouses?
5. What challenges exist for further practical implementation of moisture swing DAC systems in closed greenhouse environments?

The research process is structured in multiple phases, as shown in Figure 1.1, to answer the sub-questions and the main research question. Initially, the subject and the research approach is described in Chapter 1. Subsequently, in Chapter 2 all background information is given, including the literature review conducted to broaden the understanding of DAC techniques, moisture swing, and gather all

information related to CO_2 enrichment in greenhouses. Following with Chapter 3, the design of a moisture swing DAC system will be undertaken, involving the collection of essential sorbent information, setting up the mass balance for the model, and the techno-economical calculations. This information forms the basis for developing an one-dimensional numerical model to simulate the system performance. Next, inChapter 4, the key parameters will be varied systematically together with an analysis to assess the performance of the sorbent under different global climatic conditions. Then, the effects of different design parameters on the productivity, efficiency and water loss are analyzed in Chapter 5. In Chapter 6 a preliminary techno-economic viability analysis is performed to give an indication if it could be an economically attractive innovation. Finally, Chapter 7 contains the conclusion of the report along with recommendations for future work.

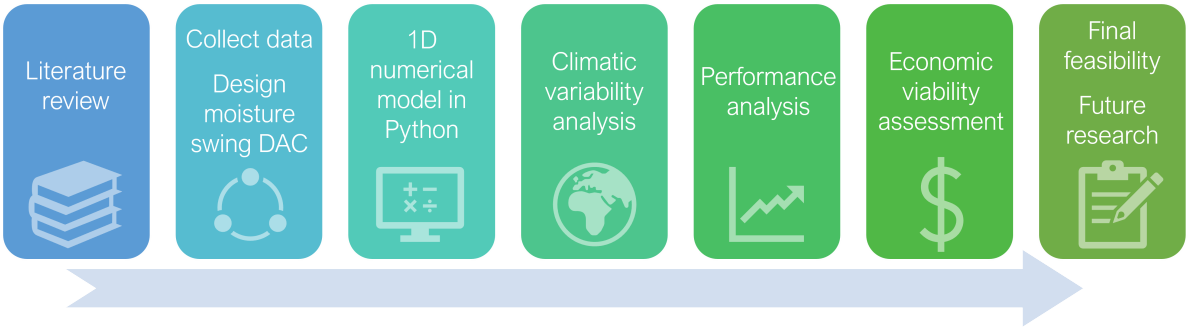

Figure 1.1: Research roadmap including the multiple phases of the feasibility study of the moisture swing adsorption system for CO_2 enrichment in a greenhouse.

2

Background Information

2.1. Climate Change

Climate change is a pressing global concern according to the Intergovernmental Panel on Climate Change (IPCC), as illustrated in Figure 2.1a the globally average land and ocean surface temperature shows a warming of 0.85°C over the period of 1880 to 2012. The temperature rise of the atmosphere and ocean is one of the main observations directly related to climate change, together with the change in the global water cycle, the acidification of the ocean, the shrink in the amounts of ice and snow around the world, and the rise of the sea level [1]. Those observations impact the ecosystems, reduce biodiversity, alter food web dynamics, reduce abundance of habitat-forming species, shift species distributions, and cause a greater incidence of disease [2, 3]. The present climate change has several causes that reinforce each other. The main causes are anthropogenic greenhouse gas emissions and deforestation, both primarily driven by human activities [1]. As illustrated in Figure 2.1b, there has been a significant rise in global anthropogenic CO_2 emissions attributed to fossil fuel-use over the past eight decades.

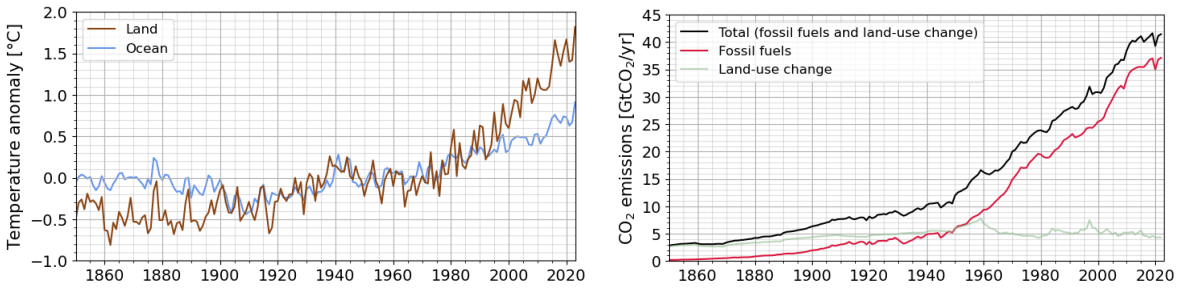

Figure 2.1: (a) Globally annual averaged combined land temperature anomaly with respect to the 20th century average (1901-2000), adapted from data of National Centers for Environmental Information [4]. (b) Global anthropogenic CO_2 emissions of the largest sources, adapted from data of Global Carbon Project - with major processing by Our World in Data [5].

Greenhouse gases (GHG) are composed of mainly carbon dioxide (CO_2), methane (CH_4), and nitrous oxide (N_2O). Around 78% of the increase in greenhouse gas emissions from 1970 to 2010 came from the CO_2 emissions of fossil fuel combustion and industrial processes [1]. The increase in anthropogenic GHG emissions in combination with other anthropogenic forcing factors, like deforestation, have caused half of the observed increase in temperature and have contributed towards the other climate changes [1]. The economic and population growth around the world is the main driver of the greenhouse gas emission increase [1].

International agreements are made to stop climate change. According to the IPCC the emission of CO_2 must be reduced by 30 to 80% by 2050 to maintain the atmospheric CO_2 concentration between 350

and 440 ppm. In 2015, 196 countries also adopted the Paris Agreement which must prevent further climate change that will have bigger impacts. The main goal of the agreement is to limit global warming to 1.5°C, which means GHG emissions must start dropping before 2025 and must be reduced by 43% in 2030 [6].

2.2. Agricultural Crop Production and CO_2 Enrichment

The climate change described earlier also affects agriculture, due to the increase in temperature the crop yield could be positively affected [7, 8] or negatively [9, 10], depending on the crop and location. Especially in poor and lesser developed countries, the food production is reduced by the climate change. This is caused mainly by increased temperatures, which will cause changing moisture regimes and droughts, shorter grain filling periods and winter chill periods, and an increase in pests and diseases [11].

The climate change together with an increasing global population poses an escalating challenge to agriculture, demanding increased crop productivity to meet escalating food demands. Mueller *et al.* [12] [12] observed that the global crop production can increase by 45 to 70%, by maximizing the crop yields. As we stand at the intersection of environmental concerns, resource constraints, and an expanding need for food security, it becomes imperative to explore innovative and sustainable solutions to increase crop productivity.

Currently, fossil fuels are used in greenhouses for heating, electricity and CO_2 enrichment. Greenhouse operators are interested in sustainable and environmentally friendly practices within the greenhouse industry to reduce their reliance on fossil fuels. Eliminating the use of fossil fuels in greenhouses will make it possible for the sector to become all-electric and rely on renewable energy only. One of the technologies that have to be implemented in a sustainable way is the CO_2 enrichment in the greenhouses.

In the agricultural sector, CO_2 enrichment is used within closed greenhouses to enhance plant growth rates and increase yields. Elevating the CO_2 concentration from 400 to 1000 ppm can effectively stimulate plant growth rates, resulting in yield increases ranging from 21 to 61 percent for both flowers and vegetables [13, 14, 15]. For tomatoes, greenhouse productivity can double in comparison to open-field cultivation, and with year-round operation, annual productivity can surge to 10 to 20 times higher levels [16]. Consequently, each square meter of land within a closed greenhouse can sequester 10 to 20 times more CO_2 from the atmosphere [17]. A study by Jung *et al.* [18] investigated the impact of the vertical position of CO_2 enrichment, concluding that strategic placement of CO_2 enrichment can enhance crop photosynthesis and improve CO_2 utilization efficiency within greenhouses. Another study by Zhang *et al.* [19] focused on the difference between conventional overall enrichment and crop-localized enrichment, with results indicating an increase in CO_2 concentration inside by 262 micromol per mol and a rise in the average leaf photosynthetic rate by 1.48 micromol per mol per second. Crop-localized enrichment exhibited an Efficiency of CO_2 Enrichment, ECE, 4.4 times higher than the conventional method. Notably, exceeding a CO_2 enrichment level of 1000 ppm typically does not result in further growth or yield increases, and may lead to detrimental effects along with increased CO_2 loss due to leakage [20]. To achieve a CO_2 concentration of 1000 ppm in a commercial greenhouse, a CO_2 injection rate of 10 to 20 kg per 1000 m^3 per hour is required [21]. The optimal range of CO_2 concentration in the air for crops is stated between 600 and 1000 ppm [22].

Commonly greenhouses are ventilated with ambient air to provide some supply of CO_2, although additional CO_2 supplementation is necessary to optimize crop growth [22]. Alternatively, CO_2 can be compressed and injected into the greenhouse to enhance growth rates and boost antioxidant capacity [23]. Many greenhouses are heated through the combustion of carbon-based fuels, a process that generates CO_2 which can be captured and used for crop cultivation, thereby also reducing carbon emissions [24, 25, 26]. Another method involves a chemical reaction between bicarbonate and acid, followed by decomposition through direct heating to obtain pure CO_2 [27]. However, this operation is complex and carries the risk of plant damage [28, 29]. Microbial fermentation of compost is yet another approach to release CO_2 for the purpose of enhancing crop growth and production [30]. Nevertheless, it comes with certain disadvantages, including the threat of ammonia poisoning [31], an unstable rate of CO_2 production [30], and the need for enough space and additional labor [32].

In a study by Wang *et al.* [33], a moisture swing adsorption technology was proposed for CO_2 delivery to greenhouses, and the adsorption isotherm and desorption kinetics were investigated. The study revealed that the resin membrane can be accurately described by the Langmuir model and can attain an adsorption capacity of 0.83 mol of CO_2 per kilogram of sorbent.

Tang *et al.* [32] investigated with a mathematical model the rotary regenerative adsorption wheel (RAW) with temperature swing for CO_2 enrichment in greenhouses. RAWs with different sorbents were investigated, respectively activated carbon, zeolite 13X and Mg-MOF-74. The study highlighted that airflow channel configuration, adsorbent choice, and mass transfer coefficient optimization are crucial factors in maximizing CO_2 enrichment performance in RAW-based systems for greenhouse applications.

2.3. Direct Air Capture

DAC is a promising carbon capture technology, which captures CO_2 directly from the ambient air and can release it to store or utilize it. DAC can be categorized into two main classes, physical and chemical. Physical capture methods rely on the physical interaction of van der Waals bonds, meaning it consumes less energy but also means the bonding is weaker making it less attractive for DAC [34]. The main disadvantage of physical capture is the small and slow uptake of CO_2 at low CO_2 partial pressures, like ambient air [35]. Chemical capture methods use a liquid or solid sorbent that chemically binds CO_2 molecules from the ambient air, and results in a strong affinity to capture CO_2 [35].

2.3.1. DAC Techniques

There are three technologies used for capturing the CO_2 directly from the ambient air:

- Absorption. Absorption is the process of dissolving CO_2 in a liquid solvent such as an aqueous amine, aqueous sodium or potassium hydroxide, ionic liquids, or a mixture of solvents [36]. Various regeneration processes can be used to capture atmospheric CO_2 and release highly concentrated CO_2 for storage or utilization.
- Adsorption. Adsorption is the binding of CO_2 onto a solid surface, such as activated carbon, zeolites, metal-organic frameworks, or amine-based solids [36, 37]. Various regeneration processes can be used to capture atmospheric CO_2 and release highly concentrated CO_2 for storage or utilization.
- Membrane separation. Membrane separation is the process where ambient air is drawn into a membrane module. The CO_2 molecules have a higher affinity for the membrane material compared to N_2 or O_2, which will result in the CO_2 molecules selectively being transported across the membrane, while the other molecules are excluded or passed at a much slower rate [38].

After capturing the CO_2 directly from the air with one of the technologies, it is necessary to release the CO_2 for storage or utilization. This is called regeneration of the sorbent, the regeneration step can be done in different ways depending on the material properties. The complete cycle of capturing CO_2 from the air and releasing it for storage or utilization can be done by pressure swing, vacuum swing, temperature swing, pressure vacuum swing, temperature vacuum swing, pressure temperature swing, moisture swing, pH swing, or salt solution regeneration.

- Pressure (or vacuum) swing. The process of pressure swing involves the adsorption of CO_2 at high pressure, followed by its desorption from the adsorbent at or around atmospheric pressure. This process typically consists of four key stages: pressurization, adsorption, depressurization, and purge [34]. The vacuum swing process is comparable, adsorption occurs under atmospheric pressure, while desorption and regeneration occur under a vacuum in this case. The energy consumption in vacuum swing is approximately 50% lower than that in pressure swing, primarily because it does not require an air compressor [39]. Vacuum swing is the most cost-effective method for handling flue gas with CO_2 concentrations ranging from 15 to 55% when operating at relatively low gas pressures [40].
- Pressure-vacuum swing. The pressure-vacuum swing process combines elements of both pressure swing and vacuum swing techniques. The adsorption phase occurs at pressures above atmospheric pressure, while the desorption step takes place under vacuum conditions. It encompasses five distinct stages: pressurization, adsorption, depressurization, evacuation, and purge.

[34]

- Temperature swing. The adsorption phase of temperature swing occurs at ambient temperature, while desorption necessitates a higher temperature, determined by the properties of the sorbent. The process comprises four distinct steps: adsorption, preheating, desorption, and precooling. [41] [34]
- Temperature-vacuum swing. The initial three steps of the temperature-pressure swing process closely resemble those of the pressure swing technique. However, following these steps, there are additional heating and cooling phases. [34]. Wilson and Tezel [42] Regeneration with temperature vacuum swing can be achieved at relatively low temperatures, typically ranging from 80 to 120°c, estimating the heat requirement for capturing each ton of CO_2 approximately in the range of 5 to 7.5 gigajoules [43].
- pH swing. Cuesta and Song [44] have described the pH swing method in detail, which comprises three primary phases: capture, regeneration, and reset. These phases cycle through three distinct surface configurations: initial, capture, and release. The pH swing technique capitalizes on the reversible chemical reactions involving CO_2 and the sorbent, allowing for efficient and reversible CO_2 capture and release [44, 45]. It allows for faster and more comprehensive CO_2 capture from the gas stream when compared to temperature swing techniques and demonstrates superior performance when compared to both temperature and moisture swing sorbents [45].
- Moisture swing. The sorbent in a moisture swing process binds CO_2 from dry air and releases it when exposed to moisture, as visualized in Figure 2.2. The key to effectively managing sorbent regeneration lies in controlling moisture levels [45].

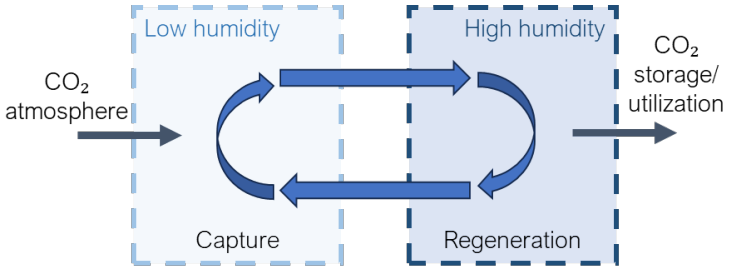

Figure 2.2: Schematic view of moisture swing CO_2 capture and regeneration process, including the change between adsorption and desorption due to a low or high humidity.

2.3.2. Commercialisation of DAC

There are currently a small amount of companies working on rolling out several DAC plants. Climeworks is working with a solid sorbent and has 14 plants with a net CO_2 removal capacity of 2,000 metric tonnes per year (t/yr) for renewable fuels, food, beverages, and agriculture, 1 commercial plant with a CO_2 removal capacity of 4,000 t/yr for CDR services, and 1 pilot plant with 900 t/yr CO_2 removal capacity for a greenhouse in Switzerland. Carbon Engineering has some plants operating with liquid sorbent, but the biggest one in Texas (USA) is under construction and is designed to capture 500,000 t/yr for carbon sequestration and for the production of low carbon products. Global Thermostat (solid sorbents) and Mechanical Tree (moisture-driven CO_2 sorbents) are two other companies in the USA working on DAC, and are mainly focusing on using it for CO_2-based fuels. Infinitree is a smaller company with a pilot plant in New York (USA) with only a CO_2 removal capacity of 100 t/yr for greenhouse application and is using ion exchange sorbent material with a humidity swing mechanism. The basic concept Infinitree used is very interesting and promising, unfortunately, it seems like the company stopped its research [46]. Using the right mechanism and finding the most suitable moisture swing sorbent could make it a useful technology in agriculture. An overview of all the companies and plants is stated in Table 2.1.

Table 2.1: Overview of current DAC plants and pilots, including their geographical location, the type of plant, the CO_2 capacity, and the sorbent regeneration type, adapted from Barbour *et al.* [46] and Ozkan *et al.* [47].

Company	Location	Plant type	CO_2 capacity	DAC type
Climeworks	Europe	14 Pilot and commercial plants	Net 2,000 t/yr	Temperature swing
Climeworks	Switzerland	Pilot plant	900 t/yr	Temperature swing
Climeworks	Iceland	Commercial plat	4,000 t/yr	Temperature swing
Carbon Engineering	Canada	Pilot plant	350 t/yr	Temperature swing
Carbon Engineering	Canada	Innovation center	1,500 t/yr	Temperature swing
Carbon Engineering	USA	Commercial plant	1,000,000 t/yr	Temperature swing
Global Thermostat	USA	Pilot plant (DAC and flue gas)	10,000 t/yr	Temperature swing
Global Thermostat	USA	Pilot plant	4,000 t/yr	Temperature swing
Global Thermostat	Chile	Pilot plant	250 kg/h	Temperature swing
Global Thermostat	USA	2 Commercial plants	Net 4,000 t/yr	Temperature swing
Mechanical Tree	USA	Prototype	30 t/tree	Moisture swing
Mechanical Tree	Global	Commercial farms	4,000 t/farm	Moisture swing
Infinitree	USA	Pilot plant	100 t/yr	Moisture swing

2.4. Moisture Swing Sorbents

Moisture swing sorbents used for DAC are usually functionalized with ammonium groups and carbonate ions, and are also called humidity swing sorbents. A CO_2 adsorption moisture swing system exhibits a preference for bicarbonate and hydroxide ions over carbonate when operating in dry conditions. This results in a higher concentration of hydroxide ions, which enhances CO_2 adsorption [48]. An example of the reactions that occur in a sorbent resin during the adsorption of CO_2 and desorption of CO_2 is shown in Figure 2.3. The fundamental reactions are the direct bicarbonate formation on the resin (Equation 2.1), the formation of carbonate (Equation 2.2), and the formation of bicarbonate from carbonate (Equation 2.3). [49]

$$OH^- + CO_2 \rightleftharpoons HCO_3^- \tag{2.1}$$

$$2OH^- + CO_2 \rightleftharpoons CO_3^{2-} + H_2O \tag{2.2}$$

$$CO_3^{2-} + CO_2 + H_2O \rightleftharpoons HCO_3^- \tag{2.3}$$

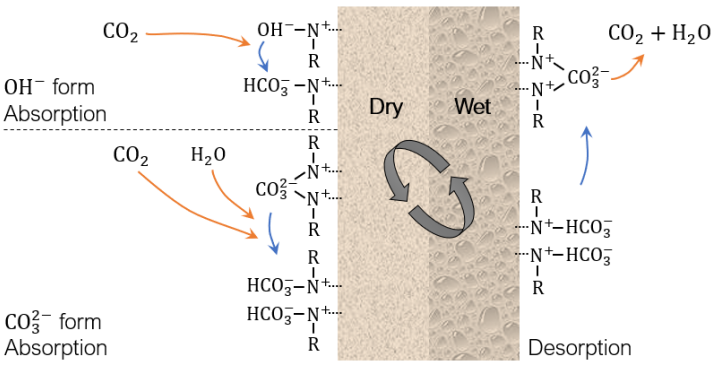

Figure 2.3: Moisture swing direct air capture sorbent including the fundamental reactions, adapted from Wang *et al.* [49].

Moisture swing sorbents regenerate through humidity oscillation instead of direct energy input, which means no cooling and heating units are required, resulting in energy savings for the adsorption system. Moreover, its adaptability allows for flexible equipment placement and the potential for complementing the system with thermal swing and vacuum units to optimize its performance [45]. Shi *et al.* [48] have explored further optimization efforts and found that using moisture swing materials with smaller pore sizes is a viable strategy for capturing more CO_2. Adjusting the particle size of silica and reducing the cation distance on its surface can increase CO_2 capacity at relatively high humidity levels. Additionally, substituting hydrophobic carbon black as a support material instead of hydrophilic polystyrene can improve efficiency in this process [48].

To achieve optimal CO_2 capture, the sorbent must exhibit excellent adsorption kinetics and a high adsorption capacity. Some of the materials used for moisture swing DAC are:

- The Excellion membrane, available commercially for moisture swing applications, consists of polypropylene co-extruded with an Excellion active resin. This active resin is a crosslinked chloromethylated polystyrene powder that has undergone quaternization with trimethylamine and ion exchange to form quaternary ammonium hydroxide groups. The Excellion membrane has a swing size of 0.12 mmol per gram and an overall adsorption/desorption rate of 2.1 x 10^{-3} mmol per minute per gram. This sorbent often serves as a reference in various experiments for comparing adsorption kinetics and capacity [50].
- Ammonium hydroxide-functionalized carbon black materials can be used for DAC with moisture swing. Under dry conditions, the bicarbonate ion is favored, with one carbonate ion absorbing one CO_2 molecule and one water molecule, resulting in the formation of two bicarbonate ions. [51].
- Colloidal crystals are three-dimensional periodic lattices formed by monodisperse spherical colloidal particles. Templates made from colloidal crystals are used in creating microporous polymers containing quaternary ammonium hydroxide groups, which can be used in humidity swing applications. [52].
- Functionalized HIPE-templated microporous polymeric materials are porous materials that have been modified through quaternization and ion-exchange reactions to introduce quaternary ammonium hydroxide groups at the pore interface. Nearly all polyHIPE materials exhibit superior reversible CO_2 capture performance compared to the commercially available Excellion membrane. [53].
- Quaternary ammonium-based resins have a high charge density and a strong binding energy. The ion exchange resin is combined with inert polyethersulfone (IER/PES), which lacks CO_2 adsorption capacity but serves as a supportive material for the resin powder. [54].
- An ion exchange resin with polyvinyl chloride as a binder (IER/PVC) shows high adsorption rates for a moisture swing system. Through the use of a thin binder and a hot water treatment, the adsorption and desorption kinetic performance can be improved. The P-100-90C sorbent has a thin PVC binder and a high diffusion rate of water molecules, which contribute to a fast kinetic performance. These moisture swing sorbents have the fastest absorption rate of CO_2 molecules from the ambient air, compared to other sorbents in the literature [55].
- A material based on the quaternization of bamboo cellulose (Q-cellulose). Quaternary ammonium groups are introduced onto a natural lignocellulose support and the study of Hou *et al.* [56] showed that extremely low or high relative humidities were not favored.
- A quaternized chitosan/poly(vinyl alcohol) hybrid aerogel (QCS/PVA) based on a widely used biomass can be used for DAC by moisture swing. The chitosan structure can be introduced with quaternary ammonium groups to provide binding sites for carbonate and bicarbonate ions. [57]

The moisture swing sorbent material, if in the right form, can be used in an adsorption system like a packed bed adsorption column or a rotary regenerative adsorption wheel. A packed bed adsorption column would need a relative low humidity during adsorption, and a relative high humidity during desorption. This could potential be implemented in a greenhouse for CO_2 enhancement as shown in Figure 2.4.

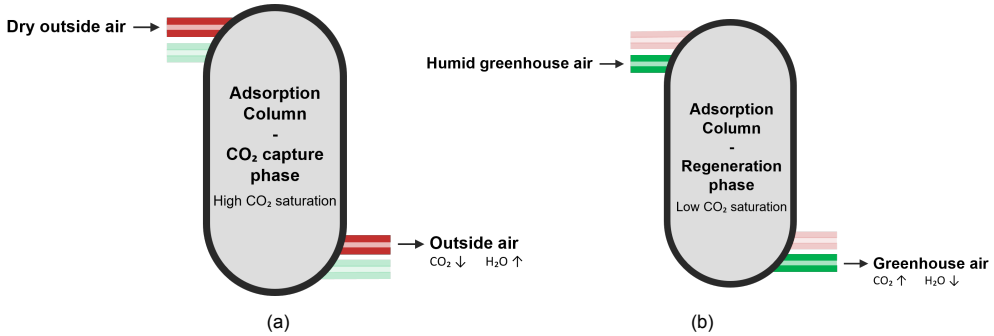

Figure 2.4: Working principle of the moisture swing system with an adsorption column, (a) the adsorption phase, and (b) the desorption phase.

2.5. Climate Regions

The moisture swing sorbents change between adsorption of CO_2 and desorption of CO_2 through a change in humidity levels. This means the water availability and the atmospheric humidity plays a crucial role. The water scarcity around the world is investigated by Molden [58], and defined four areas, little or no water scarcity, physical water scarcity, approach physical water scarcity, and economic water scarcity. In most countries the lack of investment in water or a bad infrastructure cause economic water scarcity, while physical scarcity is often caused by an arid climate of a country or an overloading of the water source [58]. Regions with physical water scarcity are lying around the tropic of cancer, like the border between Mexico and the USA, the coast of northern Africa, South-Africa, Asia, and south-east Australia. Economic water scarcity is mostly found around the equator, in a large part of Africa, Peru, Central-America, and India and a couple more countries in Southeast Asia.

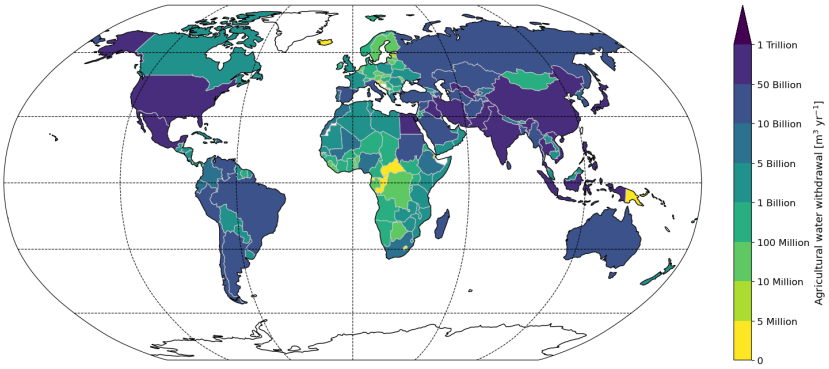

Figure 2.5: Total agricultural withdrawals in 2015, withdrawn for irrigation, livestock and aquaculture purposes, according to data of Our World in Data [59].

The working principle of a moisture swing sorbent relies on the humidity in the air, and so the geographical location. The world is characterized by diverse climate regions exhibiting variations in temperature, seasons, and humidity levels. The widely used Köppen-Geiger climate classification categorizes climates into five primary groups and several subgroups based on seasonal precipitation and temperature patterns. These main groups of Köppen were indicated on the vegetation, and are respectively tropical (A), arid (B), temperate (C), continental (D), and polar (E). The second order groups are based on the precipitation and the last tertiary groups on the atmospheric air temperature. Table Table 2.2 provides an overview of the symbols and classifications for different climate regions according to the Köppen-Geiger climate classification Peel *et al.* [60].

Table 2.2: Overview of the Köppen-Geiger climate symbols and the classifications for different climate regions, adapted from Peel *et al.* [60].

1st order group	2nd order group	3rd order group
A. Tropical climate	f. Rainforest	
	m. Monsoon	
	w. Savanna, dry winter	
	s. Savanna, dry summer	
B. Arid climate	W. Arid desert	h. Hot
	S. Semi-arid or steppe	k. Cold
C. Temperate climate	s. Dry summer	a. Hot summer
	w. Dry winter	b. Warm summer
	f. Without dry season	c. Cold summer
D. Cold snow climate	s. Dry summer	a. Hot summer
	w. Dry winter	b. Warm summer
	f. Without dry season	c. Cold summer
		d. Very cold winter
E. Polar climate	T. Tundra	
	F. Frost	

The most intriguing climate classes for a moisture swing system are those characterized by dry conditions. Therefore, arid climates such as BWh or BSh are particularly interesting, but a temperate climate like Csa is also potentially noteworthy. Figure 2.6 illustrates the global distribution of the climate regions based on the Köppen-Geiger classification. Notably, the most hypothetically favorable locations, include the Sahara, southern Africa, Australia, the Middle East, and certain small regions in North and South America.

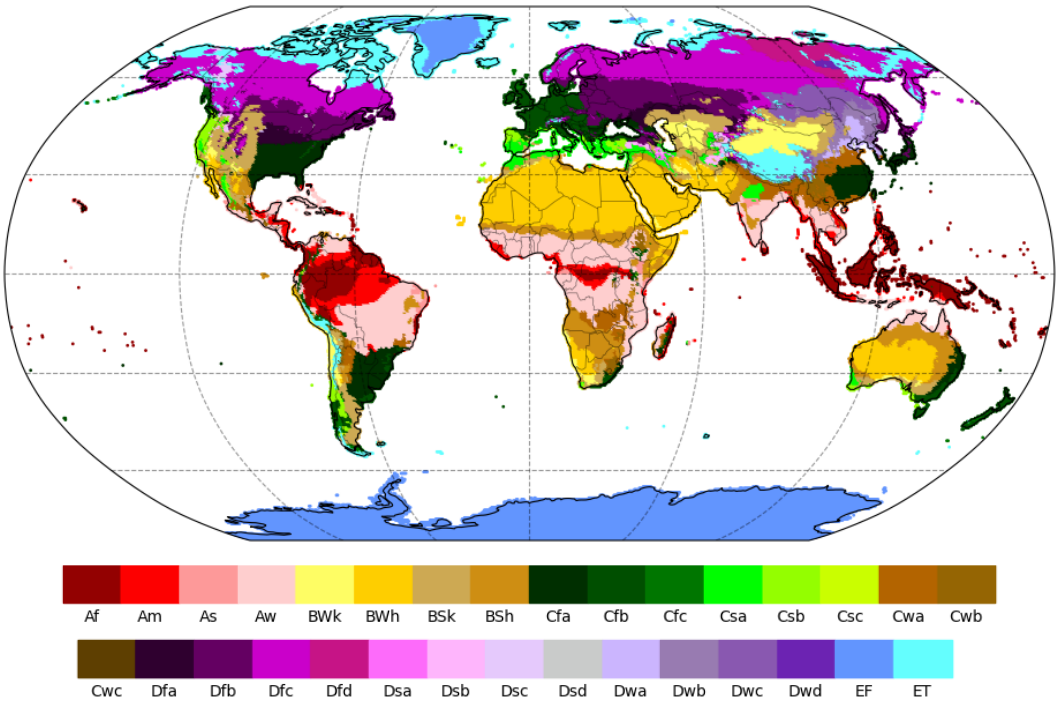

Figure 2.6: The global Köppen-Geiger climate classification map updated by Kottek *et al.* [61] with temperature and precipitation data from 1951 to 2020.

3

Methodology

3.1. Carbon Dioxide Adsorption Isotherms

The equilibrium relationship between the CO_2 gas phase concentration and the adsorbed solid phase concentration can be described by the CO_2 adsorption isotherms. These isotherms provide critical insights into the adsorption capacity of the sorbent.

The Langmuir isotherm is a fundamental model developed by Irving Langmuir and describes the chemisorption of gas molecules onto a solid surface. It assumes a monolayer coverage, where adsorption sites are occupied one at a time. According to the Langmuir model, there is a dynamic equilibrium between the adsorption and desorption of molecules onto the surface. The Langmuir isotherm is characterized by the Langmuir constant, which is a parameter representing the affinity of the gas molecules for the surface as shown in Equation 3.1.

$$\theta = \frac{q^*}{q_{\text{max}}} = \frac{K \cdot p}{1 + K \cdot p} \tag{3.1}$$

where θ [-] is the fractional coverage of the surface by adsorbed molecules (saturation of the sorbent), q^* [mol·kg^{-1}] is the adsorbed solid phase concentration of CO_2 in equilibrium with the gas phase concentration, q_{max} [mol·kg^{-1}] is the maximum CO_2 capacity of the sorbent, K [-] is the Langmuir equilibrium constant, and p [Pa] is the equilibrium partial pressure of the component in the gas.

The Gibbs free energy change is the thermodynamic driving force, a more negative Gibbs free energy change indicates a stronger affinity of the sorbent for water molecules. The relation between the Gibbs free energy and the equilibrium constant is shown in Equation 3.2.

$$\Delta G = -R \cdot T \cdot \ln(K) \tag{3.2}$$

where ΔG [J·mol^{-1}] is the Gibbs free energy change, R [J·K^{-1}·mol^{-1}] is the molar gas constant, and T [K] is the absolute temperature.

Wang *et al.* [62] suggested that the free energy change is a linear function of the relative humidity and nearly independent of the temperature. Wang *et al.* [62] fitted the saturation to a model with Equation 3.3 for the Gibbs free energy change.

$$\Delta G(T, h_r) = a + b(1 + \beta h_r)h_r + c(T - T_0) \tag{3.3}$$

where a [-], b [-], β [-] and c [-] are fit parameters from Wang *et al.* [62] in Table 3.1, h_r [-] is the relative humidity, and T_{exp} [K] is the average experimental temperature in the experiments of Wang *et al.* [62].

Table 3.1: Fit parameters a, b, β, and c of Ozkan *et al.* [47] used to determine the free energy change for CO_2 adsorption from air.

Fit parameter	a	b	β	c
Value	-31.73	12.99	0.1289	0.02578

Combining Equation 3.3 suggested by Wang *et al.* [62] for the free energy change and Equation 3.2 gives a relation of the Langmuir equilibrium constant as function of the temperature and the relative humidity.

3.2. Climatic Variability

3.2.1. Climate Regions and Conditions

The Köppen-Geiger classification defines criteria for the different climate types based on the temperature and the precipitation. While these criteria can give an indication of the minimum, maximum or mean temperature, they do not offer real-time values essential for a realistic climate analysis. Thus, locally measured atmospheric temperature data is necessary to provide more accurate results.

The atmospheric CO_2 concentrations exhibit slight seasonal fluctuations and regional variations, with a global mean value of approximately 422 ppm with a regional variation of 10 ppm. This regional variation is, according to the key parameter analysis, negligible for the CO_2 isotherm and, consequently, for the system. There are also small seasonal fluctuations each year, as shown in Figure 3.1. The Northern Hemisphere dominates the annual cycle of CO_2 concentration due to its larger land area and plant biomass. The seasonal concentration peak and drop each year is around 6 to 9 ppm, and is not significant to effect the system. Consequently, the assumption of a constant CO_2 concentration is justified, aligning with the current worldwide mean concentration of 422 ppm. This choice is further supported by the expectation that future concentrations will either stabilize or increase, ensuring a minimally variable baseline for reliable comparative results.

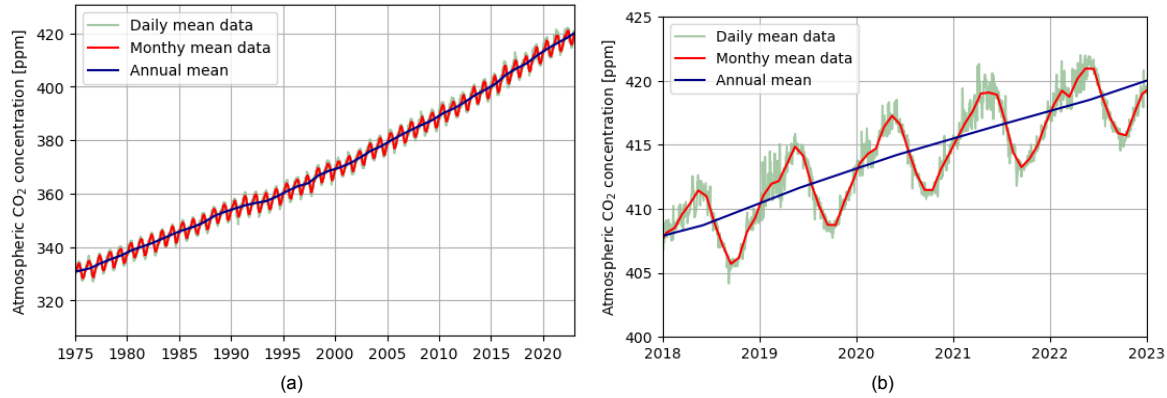

Figure 3.1: Atmospheric mean CO_2 concentration at Mauna Loa Observatory, according to data from Lan [63], (a) is from 1960 to 2023, (b) is zoomed in between 2018 and 2022.

The last and probably most critical parameter is the relative humidity of the atmosphere. As mentioned the Köppen-Geiger classification categorizes regions based only on temperature and precipitation. As precipitation alone does not directly indicate atmospheric relative humidities, and in addition, the relative humidity changes seasonally. Therefore, a global analysis of the moisture swing DAC system requires measured data on both the temperature and the relative humidity worldwide.

3.2.2. NASA Climate Data

The NASA MERRA-2 M2I1NXASM data set provides instantaneous 2-dimensional hourly data of meteorological diagnostic parameters [64]. Each file in the NASA database contains 24 hours of data for each latitude and longitude, forming an array with dimensions $24 \times 361 \times 576$. For this analysis, data of the past five years is used, focusing on temperature at 2 meters (T2M), surface pressure (PS), and specific humidity at 2 meters (QV2M).

To analyse the data, the saturation coverage as described section 3.1 is calculated. Inputs for this calculation are the relative humidity and the temperature, derived from the temperature at 2-meter data, the surface pressure, and the specific humidity at 2-meter. The Buck equation, Equation 3.4, is used to determine the saturated pressure, which helps calculate the saturated specific humidity, and finally the relative humidity with Equation 3.6.

$$p_{\text{sat}} = 0.61121 \exp\left(\left(18.678 - \frac{T}{234.5}\right)\left(\frac{T}{257.14 + T}\right)\right) \tag{3.4}$$

where p_{sat} [Pa] is the saturated pressure.

With the Buck equation, and so the saturated pressure, the saturated specific humidity can be calculated according to Equation 3.5 based on the ideal gas law.

$$h_{s,\text{sat}} = 0.62198 \frac{p_{\text{sat}}}{p_a - p_{\text{sat}}} \tag{3.5}$$

where $h_{s,\text{sat}}$ [kg·kg^{-1}] is the saturated specific humidity, and p_a [Pa] is the atmospheric pressure of air.

From the saturated specific humidity and the specific humidity at 2-meter, the relative humidity can be determind with Equation 3.6.

$$h_r = \frac{h_s}{h_{s,\text{sat}}} \tag{3.6}$$

where h_s [kg·kg^{-1}] is the specific humidity.

Using the calculated relative humidity and the temperature, the saturation coverage can be calculated for each point in the data set (24 hours a day, 361 latitude values, 576 longitude values), according to the Langmuir isotherm explained in section 3.1.

3.2.3. Year Mean Saturation and Seasonal Deviation

The CO_2 saturation at each coordinate for every hour of the day is known, with Equation 3.7 the year mean saturation can be calculated, and with Equation 3.8 the five year mean saturation can be calculated.

$$\langle\theta\rangle_y = \frac{1}{n_{h,y}} \sum_{n=0}^{n_{d,y}} \sum_{n=0}^{n_{h,d}} \theta_{h,d,y} \tag{3.7}$$

where $\langle\theta\rangle_y$ [-] is the year mean saturation coverage of the sorbent, $n_{h,y}$ [-] is the number of hours in a specific year, $n_{d,y}$ [-] is the number of days in a specific year, $n_{h,d}$ [-] is the number of hours in a day, $\theta_{h,d,y}$ [-] is the saturation coverage on a specific hour in a specific day in a specific year.

$$\langle\theta\rangle_{5y} = \frac{1}{n_{h,5y}} \sum_{n=2018}^{n=2022} \sum_{n=0}^{n_{d,y}} \sum_{n=0}^{n_{h,d}} \theta_{h,d,y} \tag{3.8}$$

where $\langle\theta\rangle_{5y}$ [-] is the 5-year mean saturation coverage of the sorbent over the period 2018 to 2022, and $n_{h,5y}$ is the total number of hours in the period 2018 to 2022.

While the mean saturation provides insights into the saturation levels for a specific year or years, the more intriguing aspects lie in understanding the seasonal variations in this year. These variations are described by the standard deviation. First for each day over the past five years, the day mean saturation is determined according to Equation 3.9. Subsequently, the seasonal standard deviation can be determined with Equation 3.10.

$$\langle\theta\rangle_d = \frac{1}{n_{h,d}} \sum_{n=0}^{n_{h,d}} \theta_{h,d} \tag{3.9}$$

where $\langle\theta\rangle_d$ [-] is the day mean saturation on a specific day, and $\theta_{h,d}$ [-] is the saturation coverage on a specific hour in a specific day.

$$\sigma^2_{\text{seasonal}} = \frac{1}{n_{d,5y}} \sum_{n=2018}^{n=2022} \sum_{n=0}^{n_{d,y}} \left(\langle\theta\rangle_d - \langle\theta\rangle_y\right)^2 \tag{3.10}$$

where $\sigma^2_{\text{seasonal}}$ [-] is the seasonal deviation over the period 2018 to 2022, and $n_{d,5y}$ [-] the number of days in the period 2018 to 2022.

3.2.4. Day-Night Shift and Diurnal Deviation

Climate conditions are dynamic and undergo variations throughout the day at any given location globally, primarily influenced by the day-night shift. This shift results in fluctuations in temperature and relative humidity. To provide a visual representation of these changes, the day-night terminator can be plotted on a map. The position of this terminator is contingent upon both the declination angle of the sun and the hour angle of the sun, representing points on the celestial sphere within the equatorial coordinate system. These angles can be precisely determined using Equation 3.11 and Equation 3.12. Spanning from -180 to 180°longitude coordinates, the latitude coordinate of the terminator for each longitude can be calculated using Equation 3.13. This approach facilitates a graphical representation of the dynamic nature of diurnal change in climate conditions, aiding in a comprehensive understanding of the impact on the CO_2 sorbent saturation.

$$\angle_{\text{dec}} = 23.45 \sin\left(\frac{2\pi}{365}(N_{\text{day}} + 284)\right) \tag{3.11}$$

where $\angle_{\text{dec}}$ [°] is the declination angle of the sun, and $(N_{\text{day}}$ [-] the day of the year.

$$\angle_{\text{hour}} = 15N_{\text{hour}} - 180 \tag{3.12}$$

where $\angle_{\text{hour}}$ [°] is the hour angle of the sun, and N_{hour} [-] is the hour of the day.

$$\text{Lat} = \frac{180}{\pi} \arctan\left(\frac{-\cos\left(\frac{(\text{Lon}+\angle_{\text{hour}})\pi}{180}\right)}{\tan\left(\frac{\angle_{\text{dec}}\pi}{180}\right)}\right) \tag{3.13}$$

where Lat [°] is the latitude coordinate of the terminator, Lon [°] is the longitude coordinate of the terminator.

To analyze the complete data of the past five years and the diurnal changes, determining the diurnal deviation is important. The diurnal standard deviation enlightens us on the alterations occurring throughout a day, attributed to the day-night shift. Unraveling these patterns enhances our comprehension of how CO_2 saturation dynamically fluctuates, contributing to a more comprehensive evaluation of the system's performance. To determine the diurnal standard deviation Equation 3.14 is used.

$$\sigma^2_{\text{diurnal}} = \frac{1}{n_{h,5y}} \sum_{n=2018}^{n=2022} \sum_{n=0}^{n_{d,y}} \sum_{n=0}^{n_{h,d}} (\theta_h - \langle\theta\rangle_d)^2 \tag{3.14}$$

where $\sigma^2_{\text{diurnal}}$ [-] is the seasonal deviation over the period 2018 to 2022, and θ_h [-] is the saturation on a specific hour.

3.2.5. Countries and Selected Cities

The world is divided into countries, which is a complex interplay of historical, political, cultural, and geographical factors. Conducting a detailed analysis of results specific to individual countries offers valuable insights into the feasibility of implementing the moisture swing system in certain countries. To enhance the practical relevance of the results, only countries with populations exceeding 1 million people are considered.

Besides the countries, an analysis is performed on some capital cities or large cities within specific countries, chosen with the assumption that they are not situated in areas with significant geographical challenges such as large mountains, unreliable electricity connections, or other highly impractical conditions for a closed greenhouse environment. The selected locations for analysis, as depicted in Figure 3.2, include those deemed interesting due to consistently high daily, monthly, and yearly mean saturations. Additionally, certain locations with remarkably lower saturation values are also considered, aiming to understand the factors contributing to the low saturation and discern the specific differences in saturation levels compared to other spots.

In North America, attention is given to Las Vegas (1) and Mexico City (2), while in South America, the focus is on São Paulo (3) and Córdoba (4). African locations include Niamey (5) and Kinshasa (6), and in Europe, Chişinău (7) and Amsterdam (8) are considered. Asian locations encompass Riyadh (9) and Chongqing (10), and in Oceania, Perth (11) and Melbourne (12) are under analyzed. These diverse locations provide a broad perspective for comprehensive analysis, allowing for insights into the variability of saturation levels and potential factors influencing them across different cities in the world.

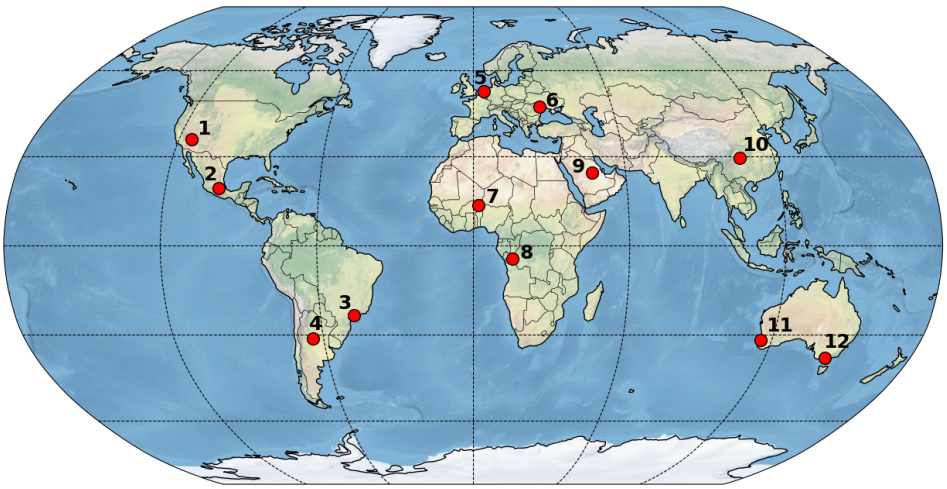

Figure 3.2: Map of the world including markers of the different analyzed cities, (1) Las Vegas, (2) Mexico City, (3) São Paulo, (4) Córdoba, (5) Niamey, (6) Kinshasa, (7) Chişinău, (8) Amsterdam, (9) Riyadh, (10) Chongqing, (11) Perth, and (12) Melbourne.

3.3. Adsorption Column Model

3.3.1. Mass Balance

A simple cylindrical adsorption column is used to analyze the feasibility before getting into more detailed engineering of the design. During adsorption, dry atmospheric air flows is used as input gas. Conversely, during desorption, moist greenhouse air is used as input gas. The adsorption column will be modeled as a gas flowing through a packed bed. A widely adopted and frequently utilized model is the axial dispersed plug flow representation of Ruthven [65], as shown in Equation 3.15.

$$\frac{\partial c_i}{\partial t} + u\frac{\partial c_i}{\partial z} - D_L\frac{\partial^2 c_i}{\partial z^2} + \left(\frac{1-\epsilon}{\epsilon}\right)\rho_s\frac{\partial \bar{q}_i}{\partial t} = 0 \tag{3.15}$$

where D_L [m^2·s^{-1}] is the axial dispersion coefficient for component i, c_i [mol·m^{-3}] is the adsorbate concentration of component i in the gas phase, z [m] is the axial distance along the bed, u [m·s^{-1}] is

the interstitial velocity through the bed, t [s] is the time, ϵ [-] is the void fraction of the bed, ρ_s [kg·m^{-3}] is the sorbent density, and $\bar{q}_i$ [mol·kg^{-1}] is the adsorbate concentration of component i in the solid phase.

The balance described by Ruthven [65] consolidates various mechanisms, containing the accumulation, the convection, the diffusion, and the adsorption. In this case, where a simple adsorption column is considered, a more intricate model with radial dispersion is generally not necessary and in many situations even ideal plug flow can be assumed.

The axial dispersion coefficient can be determined according to the Wakao-Funazkri correlation in Equation 3.16, which is valid for $3 < \text{Re} < 10^4$.

$$D_L = \frac{D_m}{\epsilon} \cdot \left(20 + \frac{1}{2}\text{Sc} \cdot \text{Re}\right) \tag{3.16}$$

where D_m [m^2·s^{-1}] is the molecular diffusivity in air, Re [-] is the Reynolds number, and Sc [-] is the Schmidt number.

The dimensionless number characterizing the mass transfer is the Sherwood number, which is the ratio between the convective mass transfer rate to the diffusion rate. Gunn [66] derived an expression that describes the dependency of the Nusselt number upon the Reynolds number and the Prandtl number, this expression can be used as a correlation for heat transfer in fixed and fluidized bed. The fluxes of heat and mass, and the mean temperatures and concentrations are analogous, which means the Sherwood number will have the same dependency, but upon the Reynolds number and the Schmidt number as in Equation 3.17. When there is radiant heat transfer contributing or a variation in physicla properties, the analogy is not correct. The Gunn correlation for mass transfer in fixed and fluidized beds applies for $\text{Re} < 10^5$ and $0.35 < \epsilon < 1.0$.

$$\text{Sh} = (7 - 10\epsilon + 5\epsilon^2)(1 + 0.7\text{Re}^{0.2}\text{Sc}^{1/3}) + (1.33 - 2.4\epsilon + 1.2\epsilon^2)\text{Re}^{0.7}\text{Sc}^{1/3} \tag{3.17}$$

The Reynolds number of a gas is the ratio between the inertial forces and the viscous forces, defined as Equation 3.18. The Schmidt number of a gas is the ratio of the kinematic viscosity and the mass diffusivity, defined as Equation 3.19.

$$\text{Re} = \frac{u d_p}{\nu} = \frac{\rho_s u d_p}{\mu} \tag{3.18}$$

$$\text{Sc} = \frac{\nu}{D_m} = \frac{\mu}{\rho D_m} \tag{3.19}$$

where d_p [m] is the sorbent particle diameter, ν [m^2·s^{-1}] is the kinematic viscosity, and μ [Pa·s^{-1}] is the dynamic viscosity.

3.3.2. CO_2 Adsorption Kinetics of the sorbent

The adsorption kinetics can be described by the linear driving force (LDF) model, as shown in Equation 3.20.

$$\frac{\partial \bar{q}_{\text{CO}_2}}{\partial t} = k_{\text{CO}_2}(q^*_{\text{CO}_2} - \bar{q}_{\text{CO}_2}) \tag{3.20}$$

where k_{CO_2} [s^{-1}] is the LDF mass transfer coefficient for CO_2, and $q^*_{\text{CO}_2}$ [mol·kg^{-1}] is the adsorbed solid phase concentration of CO_2 in equilibrium with the gas phase concentration.

The adsorbed solid phase concentration in equilibrium with the gas phase concentration can be determined according to the Langmuir isotherm described in section 3.1.

The overall mass transfer rate for CO_2 and water molecules encompasses both external (interphase) resistance and internal (intrapellet) resistance during adsorption and desorption. This overall mass transfer rate can be expressed as in Equation 3.21.

$$\frac{1}{k_{\mathrm{CO_2}}} = \frac{1}{k_{int}} + \frac{1}{k_{ext}} \tag{3.21}$$

where $k_{\mathrm{CO_2}}$ [s^{-1}] is the overall mass transfer rate of CO_2, k_{int} [s^{-1}] is the internal mass transfer rate, and k_{ext} [s^{-1}] is the external mass transfer rate.

3.3.2.1. External Mass Transfer

The external rate is determined by the transport of the adsorbate from the bulk of the gas to the external surface of the solid sorbent particles. The external surface area per unit particle volume for spherical particles can be described by three divided the radius of the particle, this means the mass transfer rate for a single-species adsorption with spherical particles becomes Equation 3.22 [67].

$$k_{ext} = \frac{6k_f}{d_p} \tag{3.22}$$

where k_f [$m \cdot s^{-1}$] is the effective mass transfer coefficient.

The effective mass transfer coefficient can be determined with Equation 3.23.

$$k_f = \frac{\mathrm{Sh} D_m}{d_p} \tag{3.23}$$

where Sh [-] is the Sherwood number.

3.3.2.2. Internal Mass Transfer

The internal rate is the transport of the adsorbate from the external surface to the internal part of the sorbent. Typical for a packed bed is the large specific surface area of the adsorbent particles, the particles are microporous, and adsorption occurs primarily within the internal void surface of the particles. So the adsorbate must diffuse into the internal part of the particles. Internal mass transfer can occur as two different mechanisms, as pore diffusion or/and as surface diffusion.

The correlation between the intrapellet diffusion coefficient and the particle phase diffusivity is given by the expression of Glueckauf [68], as described in Equation 3.24.

$$k_{int} = 60\frac{D_e}{d_p^2} \tag{3.24}$$

where D_e is the intrapellet diffusivity.

Pore diffusion occurs when the internal mass transfer relies only on the diffusion of adsorbate molecules through the pores according to Tien [67]. The effective intrapellet diffusivity can be determined from the pore diffusivity, as described in Equation 3.25, were surface diffusivity is neglected.

$$D_e = \frac{\bar{D}_p}{(\delta q/\delta c)}\frac{1}{\rho_p} \tag{3.25}$$

where $\bar{D}_p$ [$m^2 \cdot s^{-1}$] is the cylindrical pore diffusivity, and ρ_p [$kg \cdot m^{-3}$] is the pore density.

The cylindrical pore diffusivity can be determined with Equation 3.26.

$$\frac{1}{\bar{D}_p} = \frac{1}{D_p} + \frac{1}{D_K} \tag{3.26}$$

where D_p [m^2·s^{-1}] is the pore diffusivity, and D_K [m^2·s^{-1}] is the Knudsen diffusivity.

A widely acknowledged semi-empirical correlation between pore diffusivity and molecular diffusivity in the bulk gas is presented in Equation 3.27.

$$D_p = \frac{\epsilon_p D_m}{\tau} \tag{3.27}$$

where ϵ_p [-] is the particle porosity, and τ [-] is the tortuosity factor.

The tortuosity factor compensates for the fact that diffusion occurs in a zigzag pattern rather than in an straight line, and is assumed to be a typical value of 3.

Knudsen diffusion describes the diffusion that happens when the pore diameter is similar to or smaller than the average free path length of the adsorbate molecules. It can be calculated using Equation 3.28 as referenced from CITATION.

$$D_K = \frac{d_{\text{pore}}}{3}\sqrt{\frac{8RT}{\pi M}} \tag{3.28}$$

where d_{pore} [m] is the particle pore diameter, and M [kg·mol^{-1}] is the molar mass of adsorbate.

3.3.3. Water Adsorption Kinetics of the Sorbent

The adsorption kinetics of water depends on the adsorption kinetics of CO_2, and according to Wang *et al.* [62] this can be described as Equation 3.29.

$$\frac{\partial q_{\text{H}_2\text{O}}}{\partial t} = -\Delta n_w \frac{\partial q_{\text{CO}_2}}{\partial t} \tag{3.29}$$

where Δn_w [mol·mol^{-1}] is the change in water amount per mole of adsorbed CO_2.

The change in water amount per mole of adsorbed CO_2 can be calculated with Equation 3.30.

$$\Delta n_w(T, h_r) = -\frac{RT\ln K + \Delta G_a(T)}{RT\ln h_r} \tag{3.30}$$

where ΔG_a [J·mol^{-1}] is the Gibbs free energy change at a certain temperature with a relative humidity of 1.

The change in water amount per mole of adsorbed CO_2 and adsorbed solid phase concentration of CO_2 in equilibrium with the gas phase are both depending on the relative humidity. In the column the local humidity will change during adsorption and desorption, this will cause the problem that according to Equation 3.29 more water will be desorbed than the amount of water located on the adsorption sites. The assumption is made that the change in water amount per mole of adsorbed CO_2 is constant during the complete process. It is approximated to be the mean values of the change in water amount per mole of adsorbed CO_2 under outside and inside conditions, as described in Equation 3.31.

$$\bar{\Delta n_w} = \frac{\Delta n_w(T_{\text{out}}, h_{r,\text{out}}) + \Delta n_w(T_{\text{in}}, h_{r,\text{in}})}{2} \tag{3.31}$$

where $\bar{\Delta n_w}$ [mol·mol^{-1}] is the mean change in water amount per mole of adsorbed CO_2.

3.3.4. Method of Lines

The mass balance is solved using the method of lines, setting up the initial and boundary conditions, and using an integrated solver in Python. The method of lines replaces the spatial derivatives in the partial differential equation (PDE) with algebraic approximations, using finite differences. Only one derivative will remain, which means the PDE is reduced to a system of ordinary differential equations (ODEs) that approximate the original PDE. Two terms must be discretized in the mass balance, respectively the axial dispersion term and the convective flow term.

The first term in the mass balance is the axial dispersion term has to be approximated by using a second order central approximation, this is shown in Equation 3.32. From here i is used as the mesh point number.

$$\frac{\partial^2 c_i}{\partial z^2} \approx \frac{c_{i+1} - 2c_i + c_{i-1}}{\Delta z^2} + O(\Delta z^2) \tag{3.32}$$

The next term is the convective flow term which must be approximated the finite difference method. The first order upwind approximation is shown in Equation 3.33.

$$\frac{\partial c_i}{\partial z} \approx \frac{c_i - c_{i-1}}{\Delta z} + O(\Delta z) \tag{3.33}$$

3.3.5. Boundary- and Initial Conditions

To complete the statement of the problem, auxiliary conditions are specified. In t one initial condition (IC) is required, in z two boundary conditions (BCs) are required.

For the initial condition it is assumed initially there is no CO_2 or water adsorbed. Equation 3.34 shows the initial condition that states for both CO_2 and water.

$$c(z, t = 0) = \bar{q}(z, t = 0) = 0 \tag{3.34}$$

The inlet boundary condition is chosen to assume a constant feed concentration of CO_2 and water, which result in Equation 3.35 and Equation 3.36. The second boundary condition, at the outlet of the column, is assumed to be a free flow at the outlet resulting in Equation 3.37 and Equation 3.38.

$$z = 0: \quad \frac{\partial c}{\partial z} = \frac{c_{z=0} - c_{feed}}{dz} \tag{3.35}$$

$$z = 0: \quad \frac{\partial^2 c}{\partial z^2} = \frac{c_{z=1} - 2c_{z=0} + c_{feed}}{dz^2} \tag{3.36}$$

$$z = L: \quad \frac{\partial c}{\partial z} = 0 \tag{3.37}$$

$$z = L: \quad \frac{\partial^2 c}{\partial z^2} = \frac{-c_{z=N} + c_{z=N-1}}{dz^2} \tag{3.38}$$

3.3.6. Inital Value Problem Solver

The ‘scipy.integrate.solve_ivp‘ function in Python is used to numerically integrate systems of ordinary differential equations (ODEs) with given initial boundary conditions. The Backward Differentiation Formula (BDF) method is used, which is enhanced using the Numerical Differentiation Formulas (NDF) modification and offering a quasi-constant step scheme is used. The time step size is adjusted dynamically but kept relatively constant over a portion of the integration process. The solver requires a function that defines the right-hand side of these interdependent mass balance equations, allowing for precise integration over time.

3.3.7. Adsorption-Desorption Switch

A switch is implemented to change the system from adsorption to desorption, or in other words to change inlet air from ambient air to greenhouse, and vice versa. The threshold value of the switch is based on two parameters, the CO_2 concentration in the gas phase at the outlet and the CO_2 concentration in the gas phase at the inlet. The switch conditions to go from CO_2 adsorption to desorption are:

- At the inlet ($z = 0$): $c_{CO_2} = c_{\text{inside}}$
- At the outlet ($z = L_{\text{bed}}$): $c_{CO_2} \geq L_{\text{ads}} \cdot c_{\text{inside}}$

The switch conditions to go from CO_2 desorption to adsorption are:

- At the inlet ($z = 0$): $c_{CO_2} = c_{\text{outside}}$
- At the outlet ($z = L_{\text{bed}}$): $c_{CO_2} \leq L_{\text{des}} \cdot c_{\text{outside}}$

3.3.8. System Performance Indicators

To indicate the degree of saturation of the sorbent, the overall adsorbed solid CO_2 concentration of the column is determined according to Equation 3.39.

$$\bar{q}_{CO_2} = \frac{\sum_{i=0}^{i=L_{\text{bed}}} q_{CO_2,i}}{(L_{\text{bed}}/dz)} \tag{3.39}$$

where $\bar{q}_{CO_2}$ [mol·kg^{-1}] is the overal adsorbed solid CO_2 concentration of the column, and $q_{CO_2,i}$ [mol·kg^{-1}] is the local adsorbed solid CO_2 concentration at mesh point i.

The overall solid CO_2 concentration over time is shown in Figure 3.3. To determine the performance indicators it is important to analyse the adsorption-desorption cycles, which are the time intervals between two consecutive moments the system switches from greenhouse air to atmospheric air at the inlet, determined by Equation 3.40

$$t_{\text{cycle}} = t_{\text{ads2}} - t_{\text{ads1}} \tag{3.40}$$

where t_{cycle} [s] is the adsorption-desorption cycle time of the column, t_{ads1} [s] is the time step of the first switch to adsorption, and t_{ads2} [s] is the time step of the second switch to adsorption.

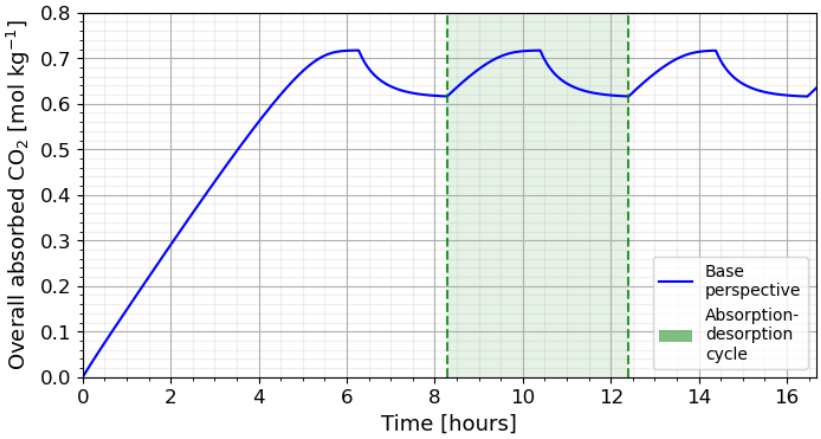

Figure 3.3: Overall solid CO_2 concentration of the entire column over time, according to the base perspective, highlighting a single adsorption-desorption cycle.

The first system performance indicator is the system efficiency of CO_2, which is the intake rate of CO_2 moving towards the greenhouse per mass of sorbent in mol per kilogram sorbent per second. This can be calculated with Equation 3.41, where the total amount of mass adsorbed per kilogram sorbent

during one cycle is divided by the cycle time. The total amount adsorbed per mass sorbent is equal to the the overall solid concentration at the top peak minus the bottom peak. The top peak is reached when the CO_2 concentrations reaches the first limit and switches from atmospheric air to greenhouse air, the bottom peak is reached when CO_2 reached the second limit and switches from greenhouse air to atmospheric air.

$$\eta = \frac{\bar{q}_{CO_2}(t = t_{des1}) - \bar{q}_{CO_2}(t = t_{ads2})}{t_{cycle}} \tag{3.41}$$

where η [mol·kg^{-1}·s^{-1}] is the system efficiency, and t_{des1} [s] is the time step of the first switch to desorption.

The next indicator is the system productivity, which is the average amount of CO_2 supplied to the greenhouse per second as determined in Equation 3.42. When using a single column the supply of CO_2 will not be constant, during CO_2 adsorption it will be zero so the productivity is an average during the cycle. The system productivity shows the total amount of CO_2 the system can supply to the greenhouse over time, which can be compared with amount of requested CO_2 to enhance the concentration in the greenhouse environment. This indicator is comparable to the efficiency only the diameter of the column will also play a significant role.

$$\dot{m}_{prod} = \eta \cdot L_{bed} \cdot \rho_s \cdot \pi \cdot \left(\frac{d_{bed}}{2}\right)^2 \tag{3.42}$$

where $\dot{m}_{prod}$ [mol·s^{-1}] is system productivity of CO_2 of the column.

Finally, the loss of water by the system can be determined by Equation 3.43, this water loss will eventually be the main input source and costs to use the system. This is the total amount of water lost in mol, at the outlet of the column during adsorption of CO_2. The water loss is related to the CO_2 utilization of the greenhouse, a higher intake to the greenhouse is a higher water usage. So to relate the water loss to the productivity, the total amount of water loss during a cycle is divided by the total amount of CO_2 moving towards the greenhouse. This can be calculated by Equation 3.44 give an amount of water loss per mol of CO_2 captured for the greenhouse utilization.

$$m_{loss} = \Phi \int_{t=t_{ads1}}^{t=t_{des1}} c_{CO_2}(z = L_{bed}) \cdot dt \tag{3.43}$$

where m_{loss} [mol] is the amount of water loss during an adsorption-desorption cycle, and Φ [m^3·s^{-1}] is the volumetric flow rate.

$$n_{loss} = \frac{m_{loss}}{\dot{m}_{prod} \cdot t_{cycle}} \tag{3.44}$$

where n_{loss} [mol·mol^{-1}] is the amount of water loss per amount of intake of CO_2.

The sensitivity analysis of the different parameters on the performance indicators is executed over a time interval of 100,000 seconds, equal to a 27.8 hours. During this interval multiple adsorption-desorption cycles will occur, the number of cycles depends on the variables of the model. The mean value of the performance indicators is calculated, together with the error during this time interval. A variation in cycles over the time interval can occur, due to the choice of solving method, where the time steps are adjusted while solving the model.

3.3.9. Base Perspective Design

The analysis of the numerical model is started from a base perspective of the adsorption column with a length of 1.0 m, which is could be a realistic size and would make it a small system to place. Axial fans can easily reach volumetric flows over 100 cubic meters per hour, which mean assuming a cylindrical column with a diameter of 0.2 m the axial velocity must be 0.88 meter per second. So in

the base perspective an axial velocity of 1.0 meter per second is chosen. The outside temperature of the atmosphere is assumed to be 20°C which is a good average temperature of a Mediterranean climate. Mediterranean climates have also good relative humidities around 0.5 which is used for the base perspective. The conditions inside the greenhouse depends on the needs of the crops, assumed in the base case is a relative humidity of 0.7 and a temperature of 22°C. As outflow limit is chosen an difference of 1% between CO_2 concentration in the inlet gas and outlet gas.

3.3.10. System Properties and Simulation Assumptions

The properties of the heterogeneous ion-exchange material Excellion I-200 are used in the model. Wang *et al.* [49] analyzed the material in the form of a flat sheet for DAC, in this report is assumed that the material can be made in the form of a packing material for in a column maintaining the same properties according to the results of Wang *et al.* [49, 62]. The density of the material in this form is unknown, the density of the majority of materials used in different adsorption columns vary between 500 to 1000 kilogram per cubic meter, so this report assumes a density of 750 kilogram per cubic meter as assumption [69, 70, 71].

Wang *et al.* [49] also analyzed the physical structure of the material with a scanning electron microscope (SEM), which provides detailed insights into the pores of the sorbent material. The images revealed the material contains pore sizes ranging from several micrometers to 50 micrometers. The Brunauer–Emmett–Teller (BET) surface area analyzer shows a surface area of 2.0 square meter per gram of sorbent. Assuming cylindrical pores this can be converted to the pore size according to Equation 3.45, giving a pore diameter of 2.67 micrometer.

$$d_{\text{pore}} = \frac{4}{A_{\text{BET}} \cdot \rho_p} \tag{3.45}$$

The properties of water and CO_2 are assumed constant and at normal temperature and pressure (NTP), which is an absolute pressure of 1 atm (101.325 kPa) and a temperature of 20°C (293.15 K). The properties of the inlet air from the atmosphere during adsorption, like the density, molar mass, dynamic viscosity, CO_2 concentration, and the atmospheric pressure are assumed constant and also at NTP.

Through the column an uniform and predefined temperature is assumed depending on the feed conditions of the outside or inside air, only the concentration changes through the column are analyzed by the mass balance. A complete overview of all properties are stated in Table 3.2.

Table 3.2: All properties necessary for the model to analyze the mass balance of the adsorption column for CO_2 enhancement in a greenhouse.

Property	Symbol	Type	Value	Unit	Reference
Molar gas constant	R	Constant	8.314	$J{\cdot}mol^{-1}{\cdot}K^{-1}$	[72]
CO_2 capacity maximum (CO_3^{2-} state)	q_{max}	Constant	0.7588	$mol{\cdot}kg^{-1}$	[49]
Temperate of experimental data	T_{exp}	Constant	288.15	K	[62]
CO_2 density	ρ_{CO_2}	Constant	1.815	$kg{\cdot}m^{-3}$	[73]
CO_2 molar mass	M_{CO_2}	Constant	$44.01 \cdot 10^{-3}$	$kg{\cdot}mol^{-1}$	[74]
CO_2 mass diffusivity	D_{m,CO_2}	Constant	$1.06 \cdot 10^{-6}$	$m^2{\cdot}s^{-1}$	[75, 76]
Outside CO_2 concentration	$c_{CO_2,\text{out}}$	Constant	422	ppm	[63]
Water density	ρ_{water}	Constant	0.998	$kg{\cdot}m^{-3}$	[77]
Water molar mass	M_{water}	Constant	$18.02 \cdot 10^{-3}$	$kg{\cdot}mol^{-1}$	[74]
Water mass diffusivity	$D_{m,\text{water}}$	Constant	$24.2 \cdot 10^{-6}$	$m^2{\cdot}s^{-1}$	[76]
Air density	ρ_{air}	Constant	1.204	$kg{\cdot}m^{-3}$	[78]
Air molar mass	M_{air}	Constant	$28.97 \cdot 10^{-3}$	$kg{\cdot}mol^{-1}$	[74]
Air dynamic viscosity	μ_{air}	Constant	$18.13 \cdot 10^{-6}$	$Pa{\cdot}s^{-1}$	[79]

Air atmospheric pressure	P_{air}	Constant	101325	Pa	[80]
Void fraction	ϵ	Constant	0.35	-	[81]
Tortuosity	τ	Constant	3.0	-	[81]
Particle density	ρ_p	Constant	750	kg·m^{-3}	[69, 70, 71]
Particle diameter	d_p	Constant	0.003	m	-
Pore diameter	d_{pore}	Constant	$2.67 \cdot 10^{-6}$	m	[49]
Pore fraction	ϵ_{pore}	Constant	0.33	-	-
Column length	L_{bed}	Variable	1.0	m	-
Column diameter	d_{bed}	Variable	0.2	m	-
Velocity	u	Variable	1.0	m·s^{-1}	-
Outside humidity	$h_{r,\text{out}}$	Variable	0.50	-	-
Outside temperature	T_{out}	Variable	0.70	K	-
Inside humidity	$h_{r,\text{in}}$	Variable	0.50	-	-
Inside temperature	T_{in}	Variable	0.70	K	-
Inside CO_2 concentration	$c_{CO_2,\text{in}}$	Variable	750	ppm	-

3.4. Techno-Economic Assessment

3.4.1. CAPEX

The successful implementation of the moisture swing DAC system within a greenhouse environment will rely heavily on the initial capital investments required for installation and production of the system. The capital expenditures (CAPEX) represent an initial investment outlay for implementing the system. The goal is to provide a first breakdown of the costs involved in designing, constructing and installing the system in the greenhouse. Additional expenses related to electrical grid infrastructure modifications or water supply systems should also be considered, but in this analysis it has been excluded from the CAPEX.

According to Towler and Sinnott [82] the fixed capital investment is split into four parts, the installing costs, offsite costs, engineering and construction costs, and contingency charges. The offsite costs, the engineering and construction costs, and the contingency costs are more important further in the design phase towards implementation at a commercial greenhouse, so for now those are neglected. Taking only in consideration the installing costs which is divided in four parts, the shell, the internal components, the auxiliary, and the fan, as described in Equation 3.46.

$$\text{CAPEX} = C_{\text{shell}} + C_{\text{internal}} + C_{\text{auxiliary}} + C_{\text{fan}} \tag{3.46}$$

where CAPEX [€] are the capital expenditures, C_{shell} [€] are the shell costs, C_{internal} [€] are the internal components costs, $C_{\text{auxiliary}}$ [€] are the auxiliary costs, and C_{fan} [€] are the costs of the fan.

Assumed the column shell will be made of carbon steel with a shell thickness of 3/8 inch and a stainless steel layer on the inner side of the column to minimize corrosion of the column. Stainless steel is necessary to prevent corrosion, but is also more expensive compared to carbon steel, so only a thin 1/4 inch layer is used to prevent corrosion. The costs of carbon steel and stainless steel can be determined with Equation 3.47 and Equation 3.48 based on formulas from Peters and Timmerhaus [83], but including an inflation index. Peters and Timmerhaus [83] used price currencies from 1990, so an inflation index of 2.43 is used to convert it to current (2024) currency [84].

$$C_{\text{carbon-steel}} = 276.1 \cdot m_{\text{outer-shell}}^{0.6016} \cdot I_{1990} \tag{3.47}$$

$$C_{\text{stainless-steel}} = 575 \cdot m_{\text{inner-shell}}^{0.609} \cdot I_{1990} \tag{3.48}$$

where $C_{\text{carbon-steel}}$ [€·kg^{-1}] is the carbon steel price, $C_{\text{stainless-steel}}$ [€·kg^{-1}] is the stainless steel price, $m_{\text{outer-shell}}$ [kg] is the mass of the outer shell, $m_{\text{inner-shell}}$ [kg] is the mass of the inner shell, and I_{1990} [-] the inflation index.

The mass of the shell is assumed to be the density of the steel times the side shell volume of the column, as described in Equation 3.49 and Equation 3.50, for respectively the outer and inner shell. The density of carbon steel and stainless steel are found in Table 3.3.

$$m_{\text{inner-shell}} = \pi \cdot L_{\text{bed}} \cdot \left(\frac{d_{\text{bed}}}{2} + t_{\text{inner}}\right)^2 - \left(\frac{d_{\text{bed}}}{2}\right)^2 \tag{3.49}$$

$$m_{\text{outer-shell}} = \pi \cdot L_{\text{bed}} \cdot \left(\frac{d_{\text{bed}}}{2} + t_{\text{inner}} + t_{\text{outer}}\right)^2 - \left(\frac{d_{\text{bed}}}{2} + t_{\text{inner}}\right)^2 \tag{3.50}$$

where t_{inner} [m] is the thickness of the inner shell, and t_{outer} [m] is the thickness of the outer shell.

The internal components of an adsorption column are considered to be distributors and the packing. Distributors are especially necessary in larger columns, in this case it is assumed distributors are not needed in the system. The packing of the bed are spherical particles made of the Excellion I-200 material, which has quaternary ammonium as the functional groups. The price of the Excellion I-200 resin from SnowPure is unavailable. Therefore, a comparable anion exchange material is used with quaternary ammonium functional groups as price indication, called Amberlite FPA90 Cl Ion Exchange Resin. This material is a strong base anion with a macroporous matrix and its physical form are off-white, opaque, spherical beads [85]. DuPont [86] produces Amberlite FPA90 Cl in bulk amount for €177.43 per kilogram.

$$C_{\text{internal}} = \rho_s \cdot L_{\text{bed}} \cdot \pi \cdot \left(\frac{d_{\text{bed}}}{2}\right)^2 \cdot C_{\text{sorbent}} \tag{3.51}$$

where C_{sorbent} [€·kg^{-1}] is the price of the adsorption material.

The auxiliary costs in this case of an adsorption column are all the pipes and valves. There are several pipes necessary in the system. Pipes from the greenhouse towards the adsorption column inlet and from the outlet back to the greenhouse, and pipes from the outside air to the inlet of the adsorption column and from the outlet back to the atmosphere. Control valves need to be installed in the pipes so the system can change the inlet air and the direction of the outlet air. Assuming the total pipe length is estimated at 20 meter and four control valves are necessary two at the inlet pipes and two at the outlet pipes. Spiral ducts made of galvanized spiral-nailed strip steel are estimated in the order of €10 per meter, depending on the diameter. Control valves are in the order of €15, depending on the diameter. The total auxiliary costs will be determined with Equation 3.52.

$$C_{\text{auxiliary}} = L_{\text{pipes}} \cdot C_{\text{pipes}} + N_{\text{valves}} \cdot C_{\text{valve}} \tag{3.52}$$

where L_{pipes} [m] is the total length of all pipes, C_{pipes} [€·m^{-1}] is the pipe price per length unit, N_{valves} [-] is the number of control valves, and C_{valve} [€] is the valve price per valve.

The last part of the installing costs is a fan to achieve a sufficient flow through the column. The initial fan costs can be deduced from the mass flow rate and the pressure drop over the column, according to Equation 3.53 from Peters and Timmerhaus [83].

$$C_{\text{fan}} = 5.1 \cdot 10^5 \cdot \left(\frac{\dot{m}}{6.2 \cdot 10^5}\right)^{0.6} \left(\frac{\Delta p}{1.03 \cdot 10^4}\right)^{0.5} \tag{3.53}$$

where $\dot{m}$ [kg·s^{-1}] is the mass flow rate through the column, and Δp [Pa] is the pressure drop over the column.

To calculate the pressure drop in the adsorption column, the Ergun equation is rewritten and used as in Equation 3.54 to determine the pressure drop inside the column.

$$\Delta p = \frac{150\mu_{\text{air}} \cdot L_{\text{bed}} \cdot u \cdot (1-\epsilon)^2}{d_p^2} \cdot \frac{(1-\epsilon)^2}{\epsilon^3} + \frac{1.75 L_{\text{bed}} \cdot \rho_{\text{air}} \cdot u^2}{d_p} \cdot \frac{(1-\epsilon)}{\epsilon^3} \tag{3.54}$$

where μ_{air} is the dynamic viscosity of air, and ρ_{air} is the density of air.

Table 3.3: Properties and prices used for the capital expenditures.

Property	Symbol	Type	Value	Unit	Reference(s)
Carbon steel density	ρ_{carbon}	Constant	7810	kg·m^{-3}	[87]
Stainless steel density	$\rho_{\text{stainless}}$	Constant	7750	kg·m^{-3}	[87]
Thickness carbon steel layer	t_{carbon}	Constant	9.525	mm	-
Thickness stainless steel layer	$t_{\text{stainless}}$	Constant	6.350	mm	-
Inflation factor 1990 to 2024	I_{1990}	Constant	2.43	-	[88]
Price Amberlite FPA90 Cl	C_{FPA90}	Constant	177.43	€·kg^{-1}	[89]
Density Amberlite FPA90 Cl	ρ_{FPA90}	Constant	700	kg·m^{-3}	[89]
USD exhange rate	-	Constant	0.92	€· \$$^{-1}$	[90]
Price ducts	C_{ducts}	Constant	10	€	[91]
Length ducts	L_{ducts}	Constant	20	m	-
Price valves	C_{valves}	Constant	10	€	[91]
Amount of valves	N_{valves}	Constant	4	-	-

3.4.2. OPEX

The effective operation and maintenance of the moisture swing system will have various operational expenditures (OPEX) crucial for the sustained performance of the system. The OPEX are the day-to-day costs for running the system. The energy consumption is in many systems the main expense, in the case of a moisture swing system the water consumption becomes a large expense of the OPEX. Due to uncertainties about the complexity of the system, a simple approach of the OPEX will be made. In this case only the costs for water and electricity are considered during operation, all other costs are considered negligible or will not be expected to play a role.

$$\text{OPEX} = C_{\text{water}} + C_{\text{electricity}} \tag{3.55}$$

where OPEX [€] are the total operational expenditures, C_{water} [€] are the costs for water consumption, and $C_{\text{electricity}}$ are the costs of electricity consumption.

Holidu [92] gathered and compared the costs of tap water in 120 cities around the world. The highest tap water price in EUR per cubic meter is found in Oslo (Norway), while the lowest price is found Riyadh (Saudi Arabia). Despite the water stress in Saudi Arabia is extremely high the price is still lower compared to a country like Norway with a low stress level. The tap water price can be used to determine the maximum costs related to the water consumption. The price of tap water can be used to determine the maximum costs associated with the water consumption. Tap water differs from irrigation water in that it is treated to meet drinking water quality standards, whereas irrigation water does not require the same level of treatment. As a result, tap water is generally more expensive compared to irrigation water.

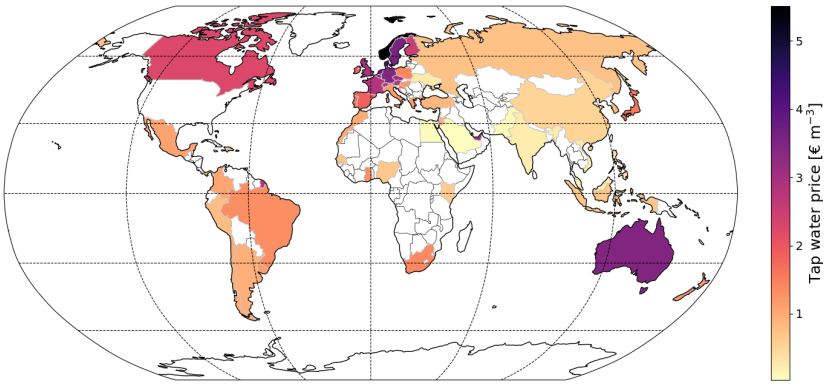

Figure 3.4: Global average country tap water price according to data of Holidu [92] including 120 cities around the world.

The actual value of irrigation water is difficult to determine, and depend on the availability, consumption, price, potential return, and quality for example. D'Odorico *et al.* [93] proposes an analysis to asses the value of irrigation water as a function of crop type and geographical location. It analysis the irrigation water value for 16 different crops, and the advantage of their approach is that is uses a mechanistic biophysical method that can be used when there are no tradable water rights existing. Looking at all major crops, the majority of the crops have a mean irrigation water value between $0.05 and $0.25 per cubic meter. Potatoes emerge as outliers with significantly greater water values due to their unique high yield characteristics and market prices. Regionally, the average irrigation water value ranges from $0.09 per cubic meter in South Asia to $0.42 per cubic meter in Europe. The global mean irrigation water value is according to the crop distribution in 2020 equal to $0.23 per cubic meter. Based on the crop that maximizes the value of irrigation water on the geographical location, the global mean irrigation water value becomes in 2020 becomes $0.71 per cubic meter. The crops analyzed by D'Odorico *et al.* [93] are mainly field crops and not greenhouse crops, still this is a good reference value of irrigation water because the water usage in a greenhouse is the same water that can be applied to field crops eventually. So, assuming a global maximized mean irrigation water value of $0.71 per cubic meter, the costs of the system can be determined. With a United States dollar (USD) inflation index from 2020 to 2024 of 1.22 [84], the irrigation water value becomes $0.87 per cubic meter. Using the USD exchange rate to euros of 0.92 according to the European Central Bank [94], the global irrigation water value can be converted to 0.80 euros per cubic meter. The molar volume of water under normal temperature and pressure (20°C and 1 bar) is 18.07 cubic centimeter per mole and together with the water loss, the water costs can be determined.

The electrical parts in the system are the fan and the control valves. Assuming the power of the control valves are negligible compared to the fan power. The fan power can be estimated from the pressure drop and the volumetric flow rate through the column according to Equation 3.56

$$P_{\text{fan}} = \Delta p \cdot \Phi \tag{3.56}$$

where P_{fan} [W] is the fan power.

To compare the electricity costs also to the efficiency of the system, the electrical fan power per amount of CO_2 intake to the greenhouse can be calculated with Equation 3.57.

$$E_{\text{fan}} = \frac{1}{3600 \cdot \eta_{\text{fan}}} \cdot \frac{V_{\text{cycle}} \cdot \Delta p}{m_{\text{cycle}}} \tag{3.57}$$

where E_{fan} [Wh·kg^{-1}] is the electrical fan power, η_{fan} [-] is the fan efficiency, V_{cycle} [m^3] is the volume of processed air, and m_{cycle} [kg] is the CO_2 mass intake to the greenhouse environment during one cycle.

The electrical power costs depends on location and also vary over time, due to inflation and country developments. GlobalPetrolPrices.com [95] retrieved the national average electricity prices of 134

countries in September 2023, which is used as a realistic price. The business electricity prices are considered, assuming a high energy intensity greenhouse of 10 hectare, which equals 2,777,778 kilowatt-hour energy consumption. The electricity prices vary a lot between countries, from 0.008 to 0.585 US dollars per kilowatt-hour, as shown in Figure 3.5. The variation is caused by the geographical location and makeup of a country, level of development, and the economy.

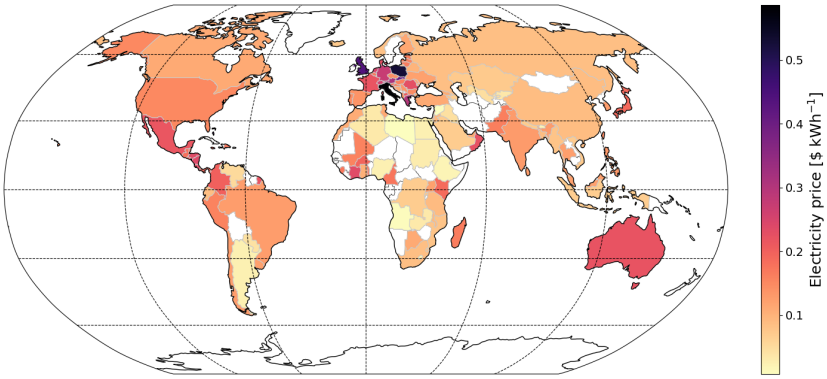

Figure 3.5: Global electricity prices for business in September 2023 according to data of GlobalPetrolPrices.com [95].

4

Climatic Variability Analysis

4.1. Gas Phase CO_2 Concentration and Relative Humidity

The CO_2 concentration in the gas significantly influences the performance of the system. The air's CO_2 concentration is one of climatic conditions that for the atmospheric air depends on the time and location, and for the greenhouse air depends on the crop's optimal circumstances to enhance the crop growth.

Figure 4.1 illustrates the CO_2 saturation of the sorbent as a function of relative humidity at a constant temperature of 20°C, with different colors representing the various CO_2 concentrations of the air. A higher CO_2 concentration in the gas phase results in a higher saturation coverage, meaning the sorbent can adsorb more CO_2. Additionally, Figure 4.1 shows the effect of the relative humidity on the efficiency of the system. The moisture sensitivity of the sorbent is highest at a high relative humidity, while the CO_2 concentration sensitivity is highest at low CO_2 concentrations. For instance, the difference in saturation coverage between relative humidities of 0.3 and 0.4 at a gas phase CO_2 concentration of 400 ppm is only 0.026, whereas between relative humidities of 0.8 and 0.9, the difference is 0.157 in saturation coverage.

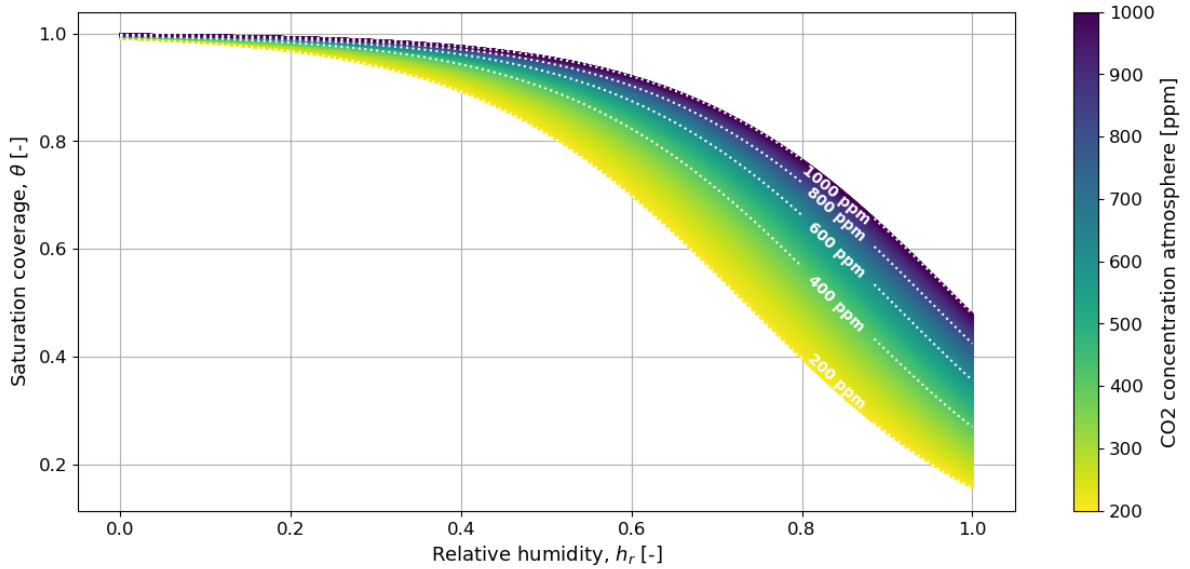

Figure 4.1: CO_2 saturation as a function of the relative humidity for different CO_2 concentrations in the ambient air at a constant temperature of 20°C.

4.2. Temperature and Relative Humidity

The temperature of the gas, along with the relative humidity and the gas phase CO_2 concentration, plays a crucial role in the efficiency of the sorbent. The adsorption of CO_2 is inversely affected by temperature. The temperature of the atmosphere depends on the time and location, and for the greenhouse air depends on the crop's optimal circumstances to enhance the crop growth, similar to the CO_2 concentration in the air.

Figure 4.2 shows the CO_2 coverage of the sorbent relative to the humidity across different temperatures, with a constant gas phase CO_2 concentration of 400 ppm. Similar to Figure 4.1, at lower relative humidities the moist sensitivity is smaller at a constant temperature. The isotherm indicates that a higher temperature reduces the saturation coverage of the sorbent at the same relative humidity. Figure 4.2 does show that the temperature sensitivity is constant for different temperatures at a constant humidity. At lower humidities the temperature sensitivity is smaller compared to higher humidities. For example, at a humidity of 0.2 the saturation difference between 30°C and 0°C is minimal, while at a humidity of 0.8 this is significant higher and equal to a difference of 0.273 in saturation coverages. From this representation, it is evident that the optimal outside atmospheric conditions are characterized by low temperatures and low humidity. In contrast, the conditions inside the greenhouse during the adsorption phase should exhibit a high humidity and a high temperature.

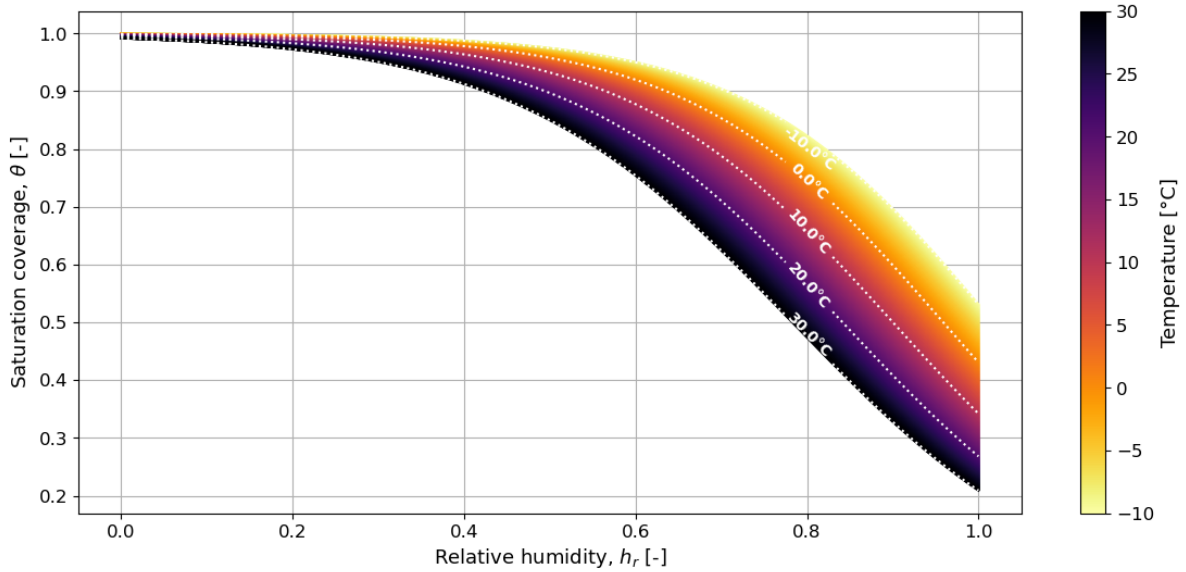

Figure 4.2: CO_2 saturation as a function of the relative humidity for different air temperatures at a constant CO_2 concentration in the air of 400 ppm.

4.3. Climate Regions and Conditions

4.3.1. Seasonal Climate Results

An overview of the world with the mean saturation on each coordinate of the past five years is shown in Figure 4.3. As mentioned in section 4.1 and section 4.2, a high saturation coverage due to outside conditions is favorable for increasing the performance of the system. As expected according to the Köppen-Geiger climate classification, the highest saturation coverages are found in the Sahara, southern Africa, Australia, the Middle East, Chile, Western United States, but also Central Asia and a part of China.

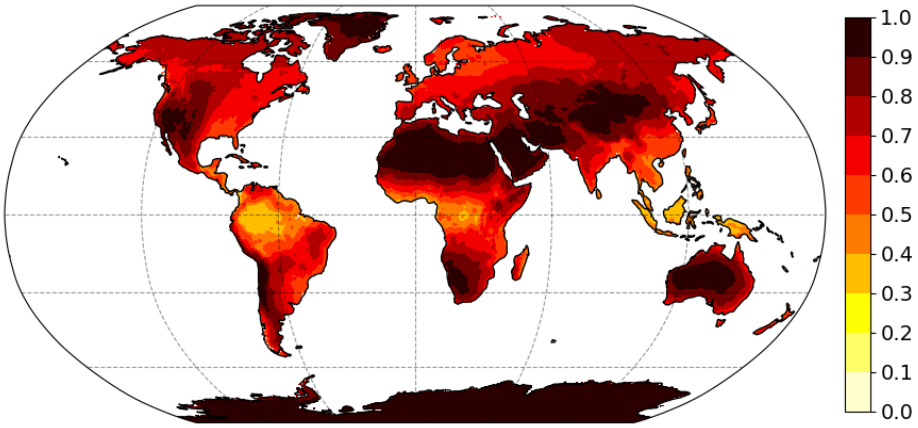

Figure 4.3: Global 5-year mean saturation according to hourly relative humidity and temperature data between 2018 and 2022 from Global Modeling and Assimilation Office [64].

The seasonal standard deviation offers valuable insights into the changes that transpire over the course of a year due to diverse seasonal weather conditions, as visualized in Figure 4.4. The largest changes are visible in regions with distinct seasons, and including a monsoon or rainy season. These regions include tropical climate countries lying along the 10°north and 10°south latitudes, such as Brazil, Nigeria, Zambia, and India. Assuming a greenhouse needs to grow crops throughout the entire year, a small seasonal deviation is preferred. This indicates a more constant saturation value throughout the year, ensuring stable performance of the system. The Sahara for example has a desirable low seasonal deviation, due to the same climate during the year.

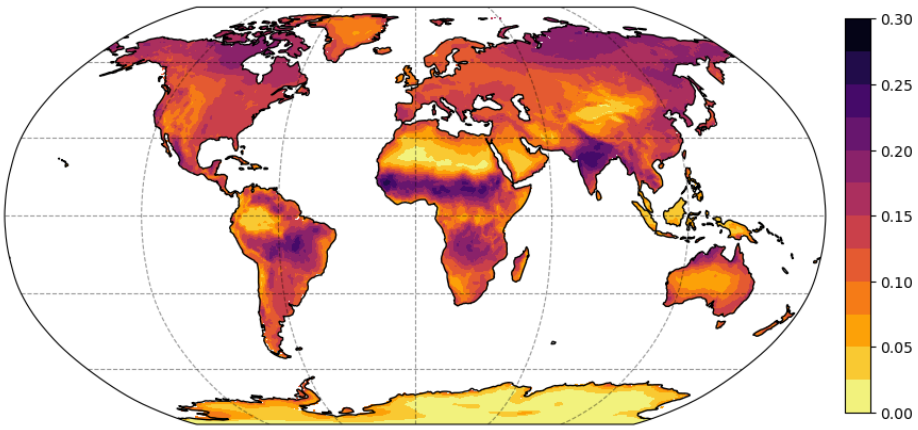

Figure 4.4: Seasonal deviation according to hourly relative humidity and temperature data between 2018 and 2022 from Global Modeling and Assimilation Office [64].

4.3.2. Diurnal Climate Results

Figure 4.5a and Figure 4.5b illustrate the saturation change between day and night on the 1st of February 2022 at a twelve-hour interval, the Northern Hemisphere experiences winter, while the Southern Hemisphere is in the summer season on this day. Notably, locations with higher saturation coverages during the day decreases less during the night compared to locations with lower saturation coverages during the day. For example, locations with a saturation between 0.8 and 1.0 exhibit minimal to almost no changes during the day-night shift, examples are the Sahara, Mexico, and the Western Coast of the USA. Regions around the equator display the most substantial changes between day and night, accompanied by notably low saturation values. For instance, Brazil, Central Africa, and Indonesia maintain a daytime saturation of approximately 0.6 to 0.7, dropping below 0.2 during the night. This intricate pattern highlights the dynamic interplay of geographic location on the diurnal variations of the saturation levels. Later in the year, in August, it is summer in the Northern Hemisphere and winter in the Southern Hemisphere. Figure 4.5c and Figure 4.5d show the CO_2 saturation at the 1st of August 2022

at respectively 00:00 and 12:00 Greenwich Mean Time (GMT). Notably, locations with lower saturation levels during daylight hours demonstrate comparatively less fluctuation than those with saturation levels nearing the maximum of 1. Prominent shifts are observable in regions such as the United States of America, Northern Brazil, Central Africa, Northern Europe, Russia, and Asia, where saturation can undergo substantial changes, ranging from approximately 0.2 to 0.5 or even higher. Conversely, locations characterized by a consistently high saturation, such as the Sahara, parts of South America, Southern Africa, and Australia, showcase minimal variability. In these areas, saturation levels remain remarkably stable, with values consistently ranging between 0.9 and 1.0 throughout the entire day.

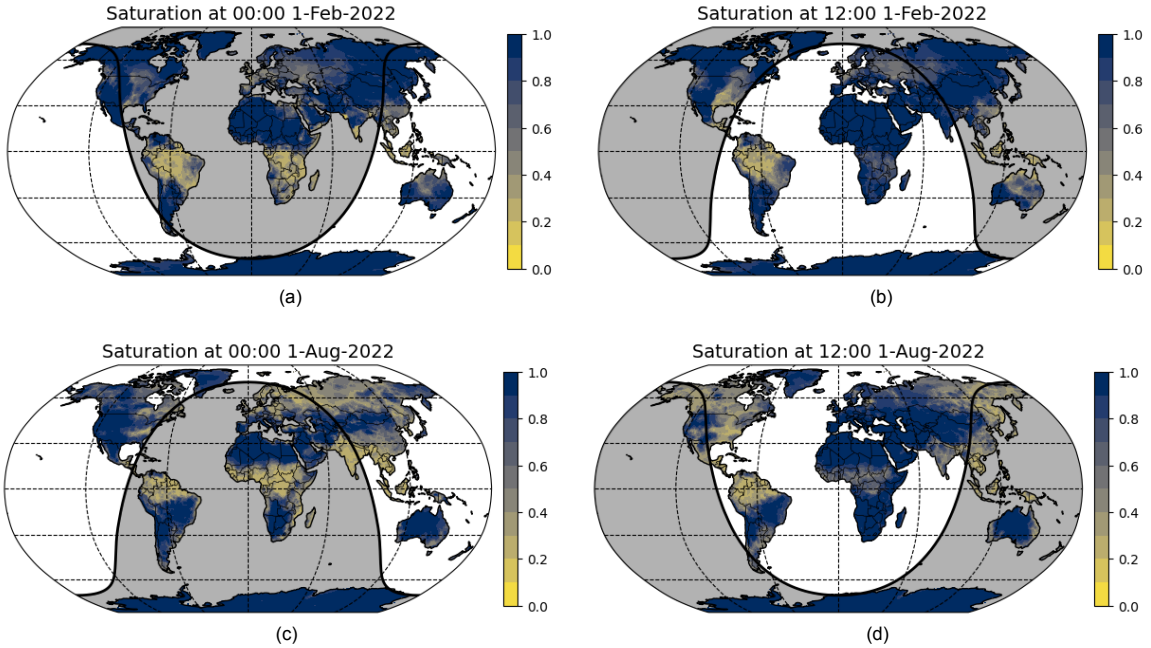

Figure 4.5: Hourly plot of the CO_2 saturation according relative humidity and temperature data from Global Modeling and Assimilation Office [64], including the day-night shift terminator, (a) is at 1 February 2022 00:00, (b) is at 1 February 2022 12:00, (c) is at 1 August 2022 00:00, and (d) is at 1 August 2022 12:00.

The diurnal deviation, shown in Figure 4.6, offer insights into the saturation change over a day due to the change from night to day light. The difference in diurnal changes around the world is smaller compared to the seasonal changes, still there are some regions with a significant smaller diurnal deviation like the Sahara and the Middle-East. Another notable observation is the higher diurnal deviation observed around the coastal areas. This coastal variation is due to factors such as the influence of the sea on the climate, and the harsher sea winds.

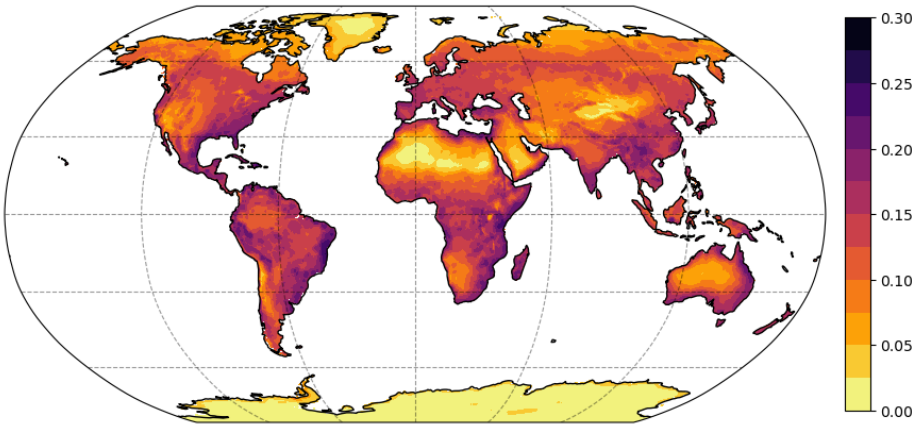

Figure 4.6: Global diurnal deviation of 2022 according to hourly relative humidity and temperature data from Global Modeling and Assimilation Office [64].

4.3.3. Country-specific Climate Results

The countries with the highest mean saturation in 2022 per continent are shown in Table 4.1. Notably, Africa and Asia are continent with significantly higher saturation values compared to North America, South America, Europe, and Oceania. The mean saturation levels in Africa and Asia surpass 0.9, while the remaining continents generally reach mean saturation coverages below 0.8 throughout 2022.

Table 4.1: The countries (written in ISO 3166-1 alpha-3 codes) with the highest year mean CO_2 saturation in 2022 according to hourly relative humidity and temperature data from Global Modeling and Assimilation Office [64], listed by continent.

North America		South America		Europe		Africa		Asia		Oceania	
USA	0.740	ARG	0.793	MDA	0.729	DZA	0.940	SAU	0.932	AUS	0.807
MEX	0.731	CHL	0.739	ALB	0.728	NER	0.926	KWT	0.921	NZL	0.558
CAN	0.727	PRY	0.710	GRC	0.723	MRT	0.925	IRQ	0.917	PNG	0.434
HTI	0.643	BOL	0.675	MKD	0.722	MLI	0.896	AFG	0.905		
JAM	0.573	URY	0.622	BGR	0.721	LBY	0.896	MNG	0.904		
DOM	0.548	PER	0.597	ESP	0.720	EGY	0.884	IRN	0.899		
JAM	0.524	VEN	0.549	ROU	0.706	NAM	0.879	TKM	0.885		
PRI	0.521	BRA	0.528	HUN	0.705	SDN	0.875	TJK	0.872		
SLV	0.488	ECU	0.497	RUS	0.701	TCD	0.871	UZB	0.861		
TTO	0.486	COL	0.427	ITA	0.699	BWA	0.856	YEM	0.859		

As example if the greenhouse environment has a temperature of 22°C, a relative humidity of 75%, and a CO_2 concentration in the air of 600 ppm, the saturation of the sorbent is equal to 0.714 for the greenhouse environment conditions. This means for a country like Australia, when only looking at the mean values over a year, the difference between atmospheric air and the greenhouse air is only 0.093, which means only $70.57 \cdot 10^{-3}$ moles of CO_2 per kilogram of sorbent is transferred from the atmospheric air to the greenhouse environment.

4.3.4. City-specific Climate Results

Figure 4.7 illustrates the monthly mean saturation values in 2022 in Las Vegas, Mexico-City, São Paulo, and Córdoba. Las Vegas exhibit minimal variation throughout the year, with only a slight change of approximately 0.1 difference between the saturation in highest saturation month May and the lowest saturation month August. In contrast, Mexico-City display more pronounced fluctuations with the highest monthly saturation of 0.9 in March, and the lowest under 0.6 in September. In São Paulo, the monthly average temperature remains consistent, ranging between 19 and 25°C. However, there is a distinct wet period from September to March and a dry period from April to August. These seasonal fluctuations are reflected in the saturation results in Figure 4.7. Córdoba, located in central Argentina, is just 1981 kilometers away from São Paulo. Despite their proximity, there are significant differences in saturation coverages. Córdoba consistently achieves a much higher monthly mean saturation coverage compared to São Paulo, due to the divergent climatic conditions between the two regions.

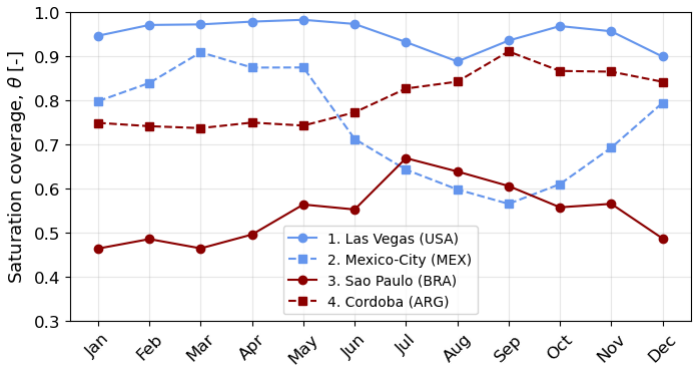

Figure 4.7: Monthly mean CO_2 saturation coverage at specific cities in North-America and South-America in 2022.

Figure 4.8 shows the monthly mean saturation values in 2022 in Amsterdam, Chişinău, Niamey, and Kinshasa. Amsterdam is characterized as a temperate maritime climate, the city has mild summers and winters. Amsterdam receives moderate rainfall throughout the year, with precipitation evenly distributed across the seasons. During the winter months, October to January, the mean saturation coverage drops to 0.5 while the rest of the year it is over 0.6. Chişinău in Moldova shows comparable results to Amsterdam only the difference between the maximum and minimum mean saturation month is larger, together with an overall higher saturation coverage during the entire year. In Niamey a hot semi-arid climate is found, this has extremely high temperatures and very little precipitation. The limited rainy season is from June to September, as Figure 4.8 shows, the saturation coverage drops drastically during this period from nearly 0.9 in May to 0.5 in September. Kinshasa, the capital city of the Democratic Republic of Congo, experiences a tropical savanna climate, this is characterized by distinct wet and dry seasons. The wet and dry seasons are slightly visible in the results, from June to September the saturation coverage is higher due to the lower humidities during the dry season.

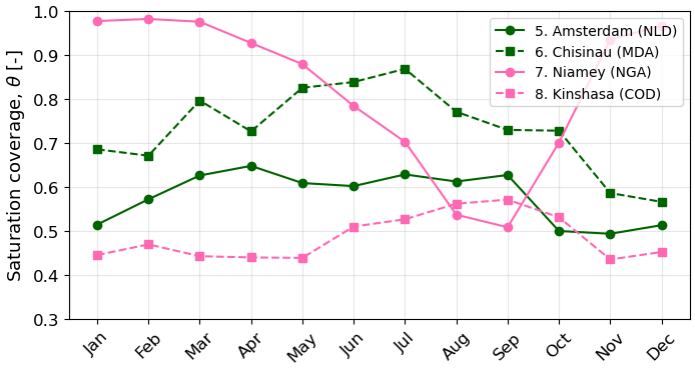

Figure 4.8: Monthly mean CO_2 saturation coverage at specific cities in Europe and Africa in 2022.

Figure 4.9 visualizes the monthly mean saturation values in 2022 for Riyad, Chongqing, Perth, and Melbourne. While Riyad, Chongqing, Perth, and Melbourne show similar monthly trends throughout the year, there are notable differences. The saturation coverage remains relatively constant over the months for most locations, with the exception of Chongqing, where fluctuations are more visible due to the monsoon season with heavy rainfall and thunderstorms. In Riyad, the monthly mean saturation coverage remains consistently above 0.9 throughout the year, except for December, when it drops to approximately 0.85. This consistency can be attributed to Riyad's hot arid climate with low humidity levels, aligning with the expected high saturation values for this climate.

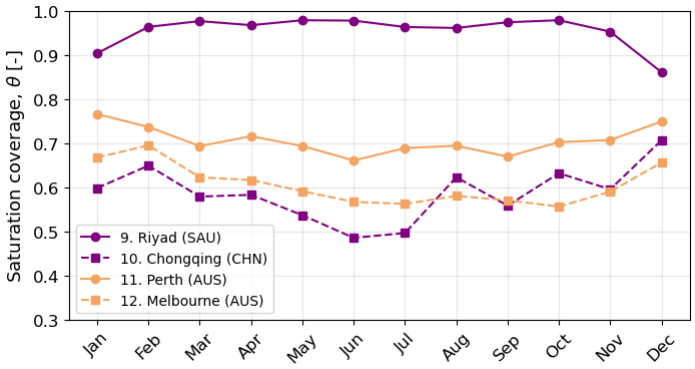

Figure 4.9: Monthly mean CO_2 saturation coverage at specific cities in Asia and Oceania in 2022.

5

Adsorption Column Performance Analysis

5.1. Gas and Solid Concentration Profiles

The adsorption and the desorption profiles of the gas and the solid concentrations give insights in the mass transfer of the molecules, where the sorbent in the column is near saturation, and the dispersion through the column.

5.1.1. Adsorption Profiles

The adsorption profile of the gas concentrations is shown in Figure 5.1. At the start of the adsorption step, the column adsorbs the most CO_2 from the gas and desorbs the most water. Figure 5.2 supports this observation, as the differences in solid concentration are more pronounced for shorter time periods compared to longer ones. Over time, the gas concentrations approach the inlet conditions, and the solid concentrations approach the saturation values of the sorbent at the inlet conditions. The opposite behavior is observed for water. As water desorbs in the column, the solid concentration of water decreases and the water flows out of the column over time. This results in water loss during the process, which is reflected in the gas concentration. Initially, the gas concentration of water is high due to the humid greenhouse air still present in the column, but over time it drops to the concentration level of the dry atmospheric air.

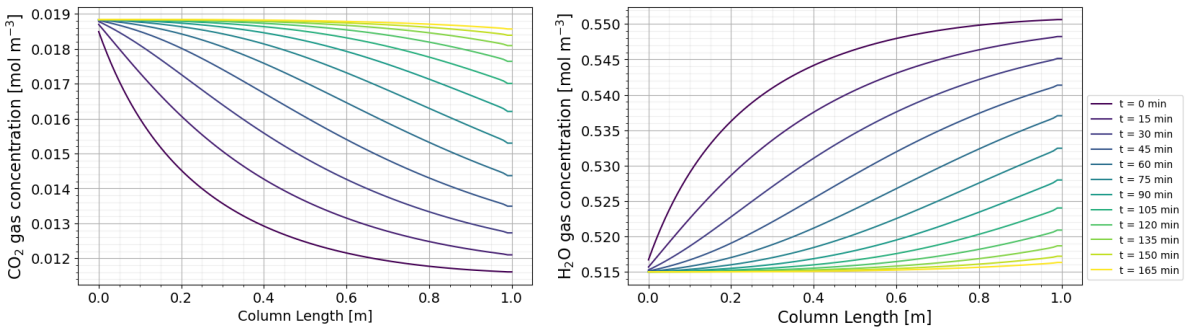

Figure 5.1: The gas phase concentration profile of CO_2 (a) and water (b) through the column during adsorption of CO_2.

The solid concentrations at the sorbent are shown in Figure 5.2. During the initial stages of adsorption, there is a rapid increase in the solid concentration of CO_2 at the beginning of the column, which then drops to nearly the initial concentration further along the column. As the adsorption time period increases, the solid concentration of CO_2 becomes more evenly distributed throughout the column, with even the end of the column showing a rise in CO_2 concentration. At longer adsorption periods, such

as 75 minutes, two distinct regions emerge: one at the beginning of the column where the sorbent is nearly fully saturated, and another where mass transfer occurs. The reverse happens for water, where in the beginning all adsorption sites are filled with water and over time the solid concentration of water drops to the equilibrium saturation line.

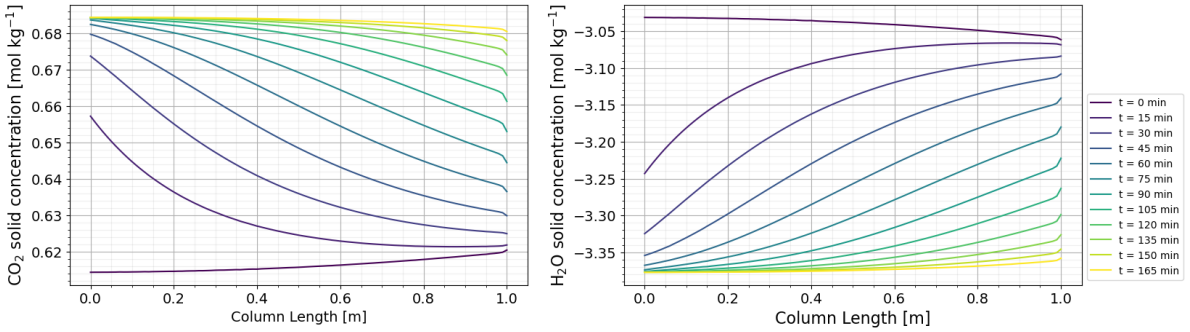

Figure 5.2: The profile solid sorbent phase concentration profile concentration of CO_2 (a) and water (b) through the column during adsorption of CO_2.

5.1.2. Desorption Profiles

The desorption gas profile of CO_2 and adsorption of water in the adsorption column are illustrated in Figure 5.3. At the start of the desorption step, the column desorbs the most CO_2 from the sorbent and simultaneously adsorbs the most water. Initially, the gas concentration of CO_2 is higher at the beginning of desorption, reflecting the release of CO_2 from the sorbent. This is evident in Figure 5.3a, where also the CO_2 concentration in the gas decreases most rapidly at the beginning of the desorption process due to the outflow of the desorbed CO_2 to the greenhouse environment. Over time, the gas concentrations approach the inlet conditions. For water, the opposite behavior is observed. In the beginning the most water is adsorbed, so the gas concentration of water is initially lower and will increase over time to the concentration level of the dry atmospheric air. This is shown in Figure 5.3b, where the water concentration in the gas starts higher but gradually drops.

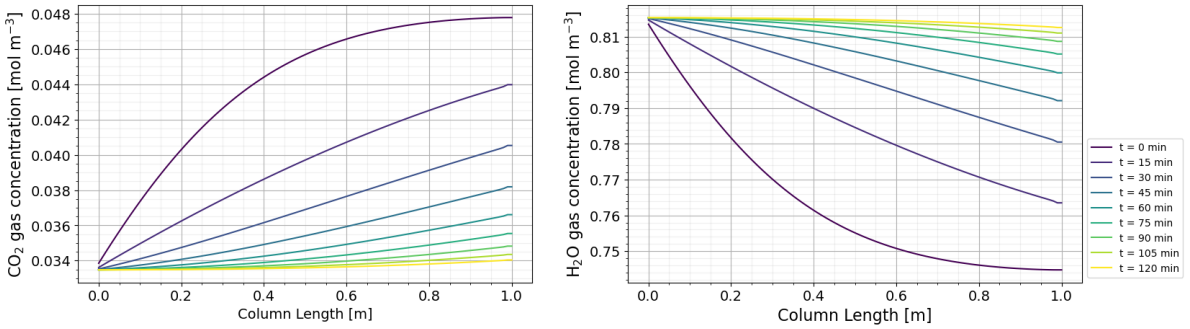

Figure 5.3: The gas phase concentration profile of CO_2 (a) and water (b) through the column during desorption of CO_2.

In the solid phase, Figure 5.4 illustrates that during the initial stage of desorption, the concentration of solid CO_2 matches the saturation concentration of the outdoor air observed during adsorption. At the beginning of the desorption process, the sorbent releases the most CO_2, as evidenced by the steep decline in concentration lines. Over time, these lines converge towards the saturation concentration, in accordance with the isotherm and the conditions within the greenhouse environment. Conversely, water starts at an initial low solid concentration that aligns with the atmospheric saturation concentration. This concentration then increases, eventually converging to the solid saturation concentration based on the conditions inside the greenhouse environment.

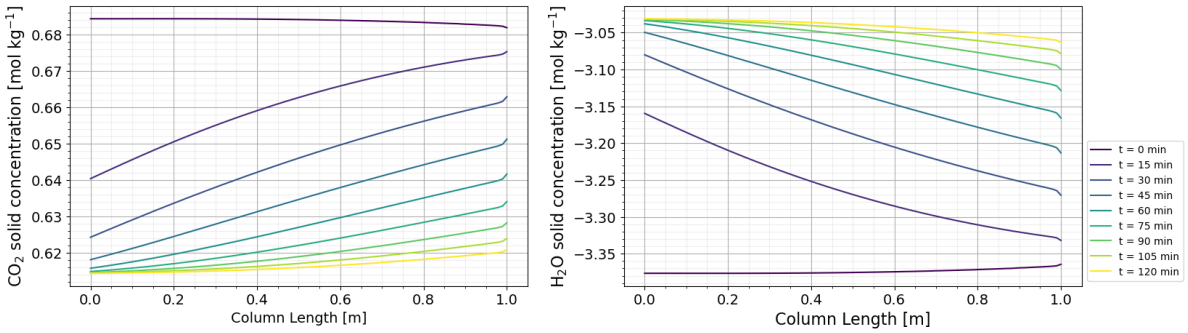

Figure 5.4: The profile solid sorbent phase concentration profile concentration of CO_2 (a) and water (b) through the column during desorption of CO_2.

5.2. System Performance

5.2.1. Shape of the Column

The shape of the column will not only determine the mass and size of the column, it will also directly affect the rate of CO_2 intake into the greenhouse. So, important is to analyze what happens when the diameter and the length of the column changes, and eventually to find an optimal and realistic shape.

The length of the column affects the mass transfer zone, and determines the contact time between the air and the adsorbent. Increasing this residence time of the air inside the column could enhance the efficiency of the column when the adsorption process is slow or when the adsorbate concentrations in the air are small. Figure 5.5a illustrates the results of the numerical model for the system efficiency of the column with different bed lengths. While decreasing the column length significantly increases the system efficiency, as shown in Figure 5.5b, it also results in increased water loss. The increase in efficiency is due to the enhanced effective use of the column. The ambient air has a low CO_2 concentration from which most CO_2 is adsorbed at the beginning of the column, which means in the rest of a larger column the gas phase CO_2 concentration is dropped and almost no CO_2 adsorption occurs. As can be observed from the concentration profiles, this happens especially at the beginning of the adsorption step. Reducing the bed length is beneficial for the system efficiency but has a drawback on the water consumption, due to the number of times the system switches between adsorption and desorption increases over the time period. Each time the adsorption step starts, there is still humid greenhouse air inside the column and this will flow to the atmosphere, resulting in extra water loss. The more times the adsorption step is initiated, the more water will be lost. When water availability is high and its cost is low, decreasing the column length is advantageous due to the efficiency gain. Increasing the bed length, changes in lengths stop to have impact on the system, converging to an efficiency of between 2 and 3 moles of CO_2 per kilogram sorbent. This stagnation is due to the fact that the largest changes in concentrations parts occur during the initial stages at the inlet up to 0.6 m into the column, increasing the overall length will decrease the impact of this first section of the column on the overall efficiency.

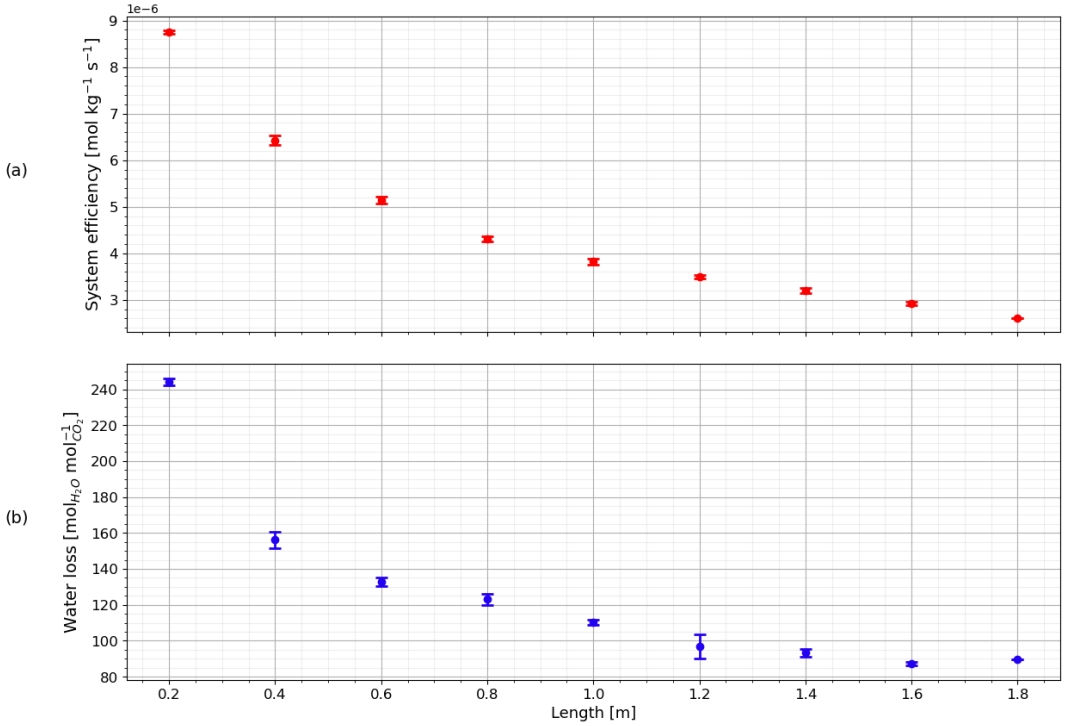

Figure 5.5: The mean performance (and errors) of the adsorption-desorption cycles of the system for different column lengths, with (a) the system efficiency, and (b) the water loss of the system.

The diameter of the column determines the surface area, with a larger surface area correlating to a higher adsorption capacity. Additionally, it influences the necessary fan power, as increasing the diameter results in a lower flow velocity for a given flow rate. Increasing the diameter improves adsorption capacity but also necessitates increased fan power to maintain the same velocity. Figure 5.6 depicts the productivity in terms of moles of CO_2 per second moved into the greenhouse environment. According to Esmeijer [96], greenhouse crops require 40 to 80 cubic meters of CO_2 per hectare per hour, equivalent to 0.5 to 1.0 moles of CO_2 per second per hectare of greenhouse. The baseline column, with a length of 1.0 meters and a diameter of 0.2 meters, achieves a CO_2 intake of only $90.07 \cdot 10^{-6}$ moles per second. To meet the required input of 0.5 moles per second, 5551 adsorption columns would be necessary per hectare of greenhouse. Although increasing the diameter boosts the CO_2 intake rate, it significantly raises water loss during the adsorption-desorption cycle but will be necessary to decrease the amount of adsorption columns.

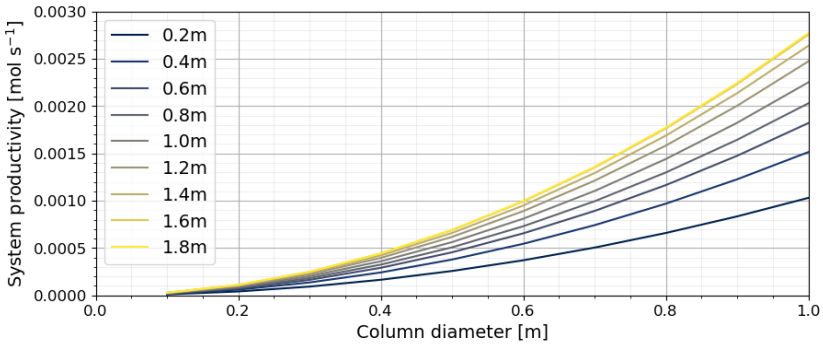

Figure 5.6: The mean productivity of the adsorption-desorption cycles of the system for different column lengths and diameters.

5.2.2. Velocity of the Gas

The velocity of the gas impacts the distribution of the adsorbate concentration throughout the column, influencing the rate at which adsorbate molecules contact the adsorbent surface. Systems with limited mass transfer resistance benefit from higher gas velocities, as this leans to faster adsorption rates and greater adsorption efficiencies. However, higher velocity results in a shorter residence time, which reduces the duration available for adsorption to occur. Additionally, changing the velocity affects the fan power required to achieve this velocity, if the shape of the column is kept constant. A change in the velocity will change the external mass transfer coefficient and the axial dispersion coefficient, and affects the convection term in the mass balance.

Figure 5.7 illustrates the system efficiency and water loss at various gas velocities. Both system efficiency and water loss increase with higher gas velocities through the column. Increasing the velocity will create a more dispersed flow, which results in the adsorption section of the column becomes larger and the CO_2 will be adsorbed more uniform, especially for longer columns. Besides this observation, an increase in velocity results also in a shorter adsorption-desorption cycle time, which means the systems switches more frequently from adsorption to desorption resulting in a higher water loss. Increasing the gas velocity could be advantageous in scenarios where water availability is high and the costs for water are low.

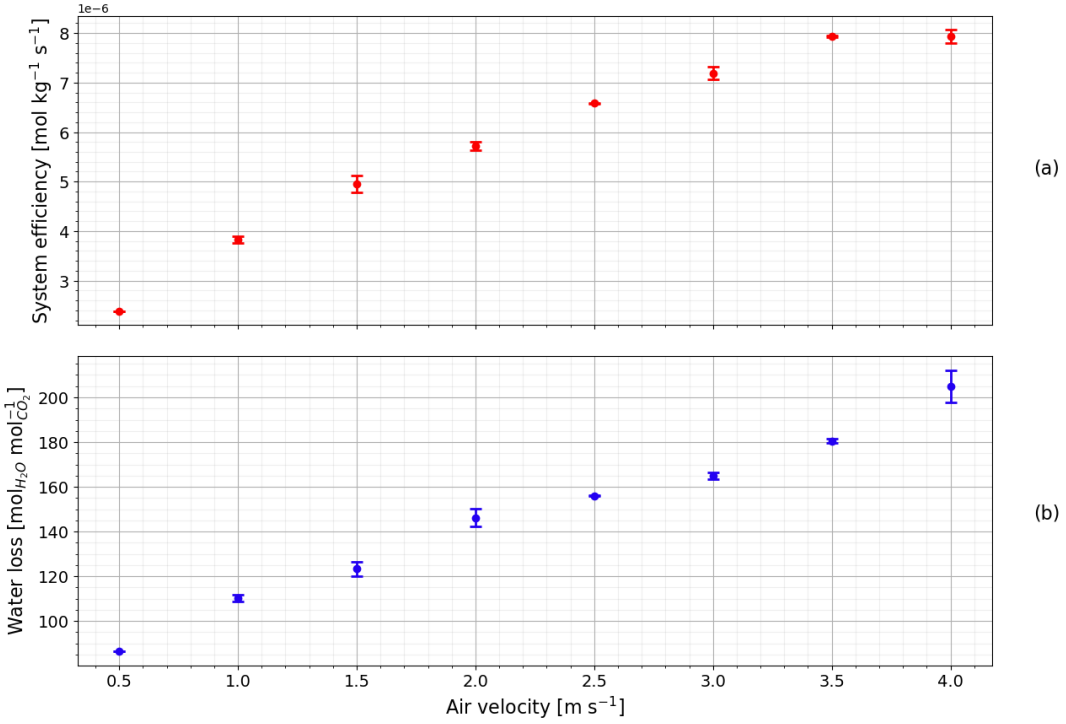

Figure 5.7: Mean system efficiency and water loss of the adsorption-desorption cycle for different velocities, including the error.

5.2.3. Atmospheric and Greenhouse Conditions

The outside and inside temperatures, the CO_2 concentration in the air, and the water concentration in the air, both in the atmosphere and the greenhouse environment, significantly impact the sorbent capacity and the intake rate into the greenhouse.

The outside relative humidity is a crucial parameter, influenced by geographical location and climate, and is identified as the most limiting factor in the system according to the key parameter analysis. Figure 5.8 illustrates the system efficiency and water loss for different outside relative humidities. The system efficiency decreases linearly with increasing outside relative humidity, while the water loss increases exponentially. An increase of the efficiency for lower outside humidities is the result of a larger difference in saturation capacities of the sorbent for the outside and inside conditions. As also described by the Langmuir isotherm, the sorbent adsorbs more CO_2 from the air at lower humidities over

the same time period. The increase of water loss is interesting, because the number of adsorption-desorption cycles over the same time period does not increase with increasing the outside humidity. The water loss is caused as a result of a higher mean change in amount of water per mole of adsorbed CO_2, which is proportional to the inverse natural logarithm of the relative humidity. This causes the sorbent to desorb more water for the same amount of CO_2 adsorbed. As expected, a low relative outside humidity is desirable, providing the highest efficiency and the lowest water loss. The smaller difference in saturation capacities between outside and inside conditions, for a higher outside humidity, causes a larger error in the water loss. The smaller difference causes smaller changes over time, which made the solver to use larger time steps, which decreased the accuracy.

The impact of the relative humidity inside the greenhouse on the system efficiency is shown in Figure 5.9a, which demonstrates a linear increase. Figure 5.9b shows an exponential decrease in water loss with increasing inside relative humidity. The effect of the inside humidity is the inverse of the outside temperature. The increase in efficiency is a result of the increased difference in saturation capacity of the sorbent between the outside and inside conditions. The mean change in amount of water per mole adsorbed CO_2 is not the determining factor of the water loss. The decrease cycle time is the dominant factor, causing the system to switch more often, which results in more water released to the atmosphere. Therefore, maintaining a high relative humidity inside the greenhouse minimizes the water loss and maximizes the system efficiency. The larger error in water loss for a lower humidity is a result of the small difference in saturation capacities between outside and inside conditions, which causes small changes in concentrations. The small changes over time cause the solver to use larger time steps, which decreased the accuracy.

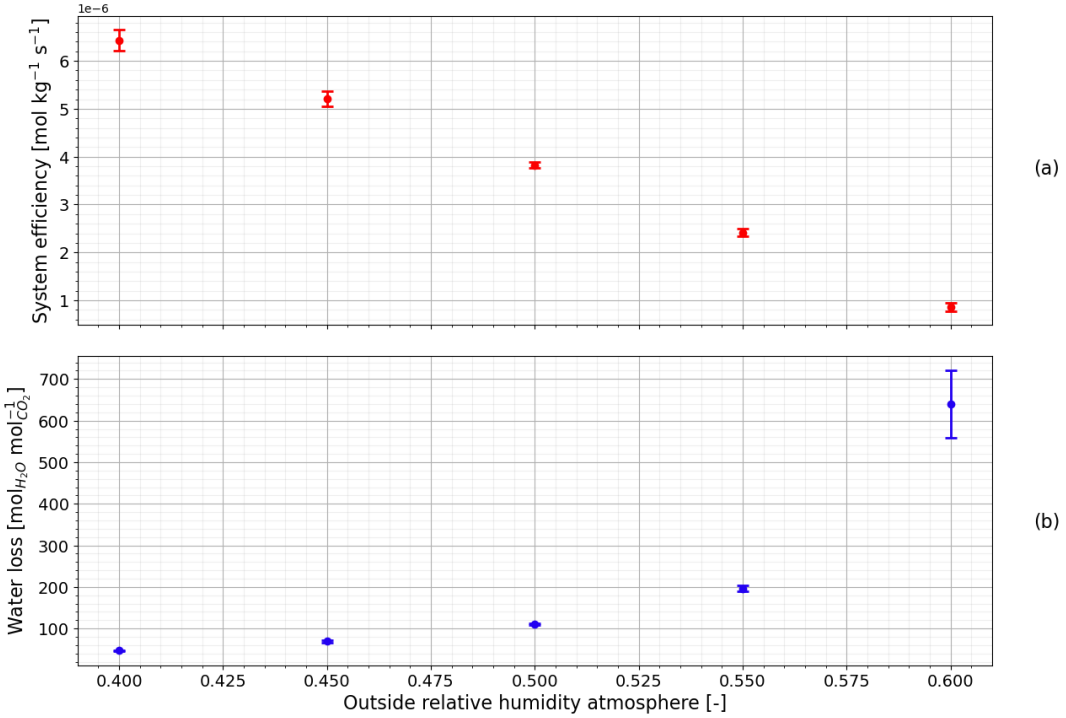

Figure 5.8: Mean system efficiency and water loss of the adsorption-desorption cycle for different outside relative humidities, including the error.

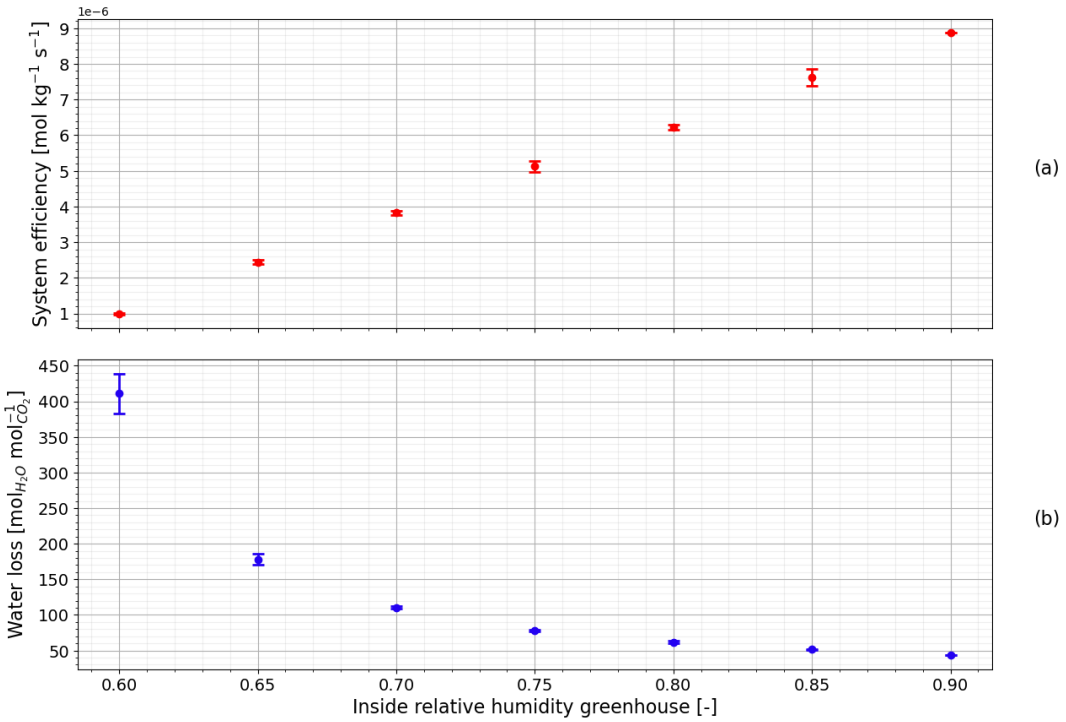

Figure 5.9: Mean system efficiency and water loss of the adsorption-desorption cycle for different inside relative humidities, including the error.

The effect of the outside temperature of the atmosphere on the system efficiency is presented in Figure 5.10a, and its effect on the water loss is shown in Figure 5.10b. The outside temperature is primarily determined by geographical location and local climate. The system efficiency decreases linearly with increasing outside temperature, while water loss grows exponentially. A higher outside temperature creates comparable to the outside relative humidity a smaller difference between the saturation capacities of the sorbent for the inside and outside conditions. The decreased difference in saturation capacities causes the system to switch more often and so more water is lost. The efficiency decrease because the adsorption of CO_2 goes relatively slower and the total amount of CO_2 which the column can adsorbed is also smaller. Thus, lower outside temperatures are preferable for optimal system performance.

Figure 5.11 shows the effects of the inside temperature of the greenhouse environment on the system efficiency and the water loss, respectively. The greenhouse temperature, typically ranging between 20 and 30 degrees Celsius for most crops, shows a linear increase in system efficiency with rising temperature. Concurrently, water loss decreases linearly within this range. The inside temperature shows similarities with the inside humidity, and has the opposite effect compared to the outside temperature. The increased efficiency is due to the larger difference in saturation capacities of the sorbent between the outside and inside conditions, which causes faster adsorption and desorption of CO_2 and the overall amount of CO_2 the column can adsorb increases. The water loss reduces due to a bit lower change in water amount per adsorbed CO_2, but mainly due to a a smaller amount of cycles over a time period. Therefore, a higher inside temperature is beneficial for both system efficiency and water loss.

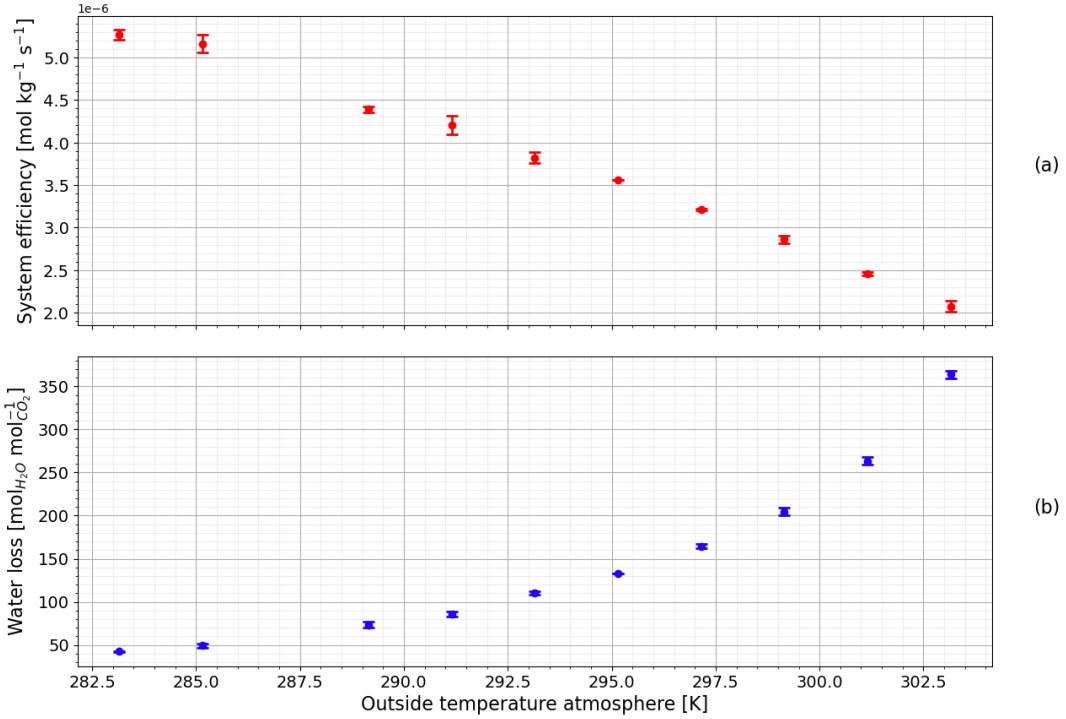

Figure 5.10: Mean system efficiency and water loss of the adsorption-desorption cycle for different outside temperatures, including the error.

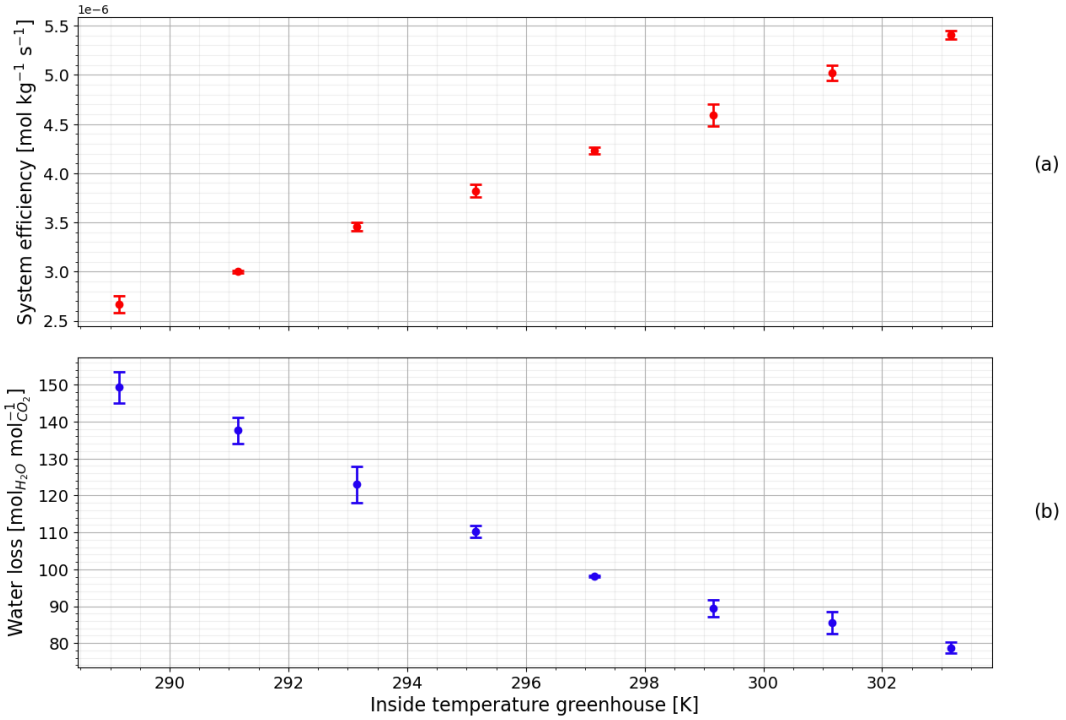

Figure 5.11: Mean system efficiency and water loss of the adsorption-desorption cycle for different inside temperatures, including the error.

The effect of the CO_2 concentration in the greenhouse air on the system efficiency and the water loss is shown in Figure 5.12. Enhanced concentrations between 600 and 1000 ppm improve crop yield for most crops. Within this range, the system efficiency decreases linearly, while the water loss increases linearly. The inside CO_2 concentration is interesting because this has no effect on Equation 3.31, which means the change in water loss is determined by the changes between adsorption and desorption. Increasing the feed concentration decreases the difference in saturation capacities of the sorbent for the outside and inside conditions, similar as the effect of the outside humidity and the outside temperature. The decreased cycle time in combination with slower adsorption and desorption kinetics causes an increased water loss and a decreased efficiency. Hence, although lower CO_2 concentrations are advantageous for the system, this is not desirable as the goal of the system is to enhance the concentration inside the greenhouse to improve crop yield.

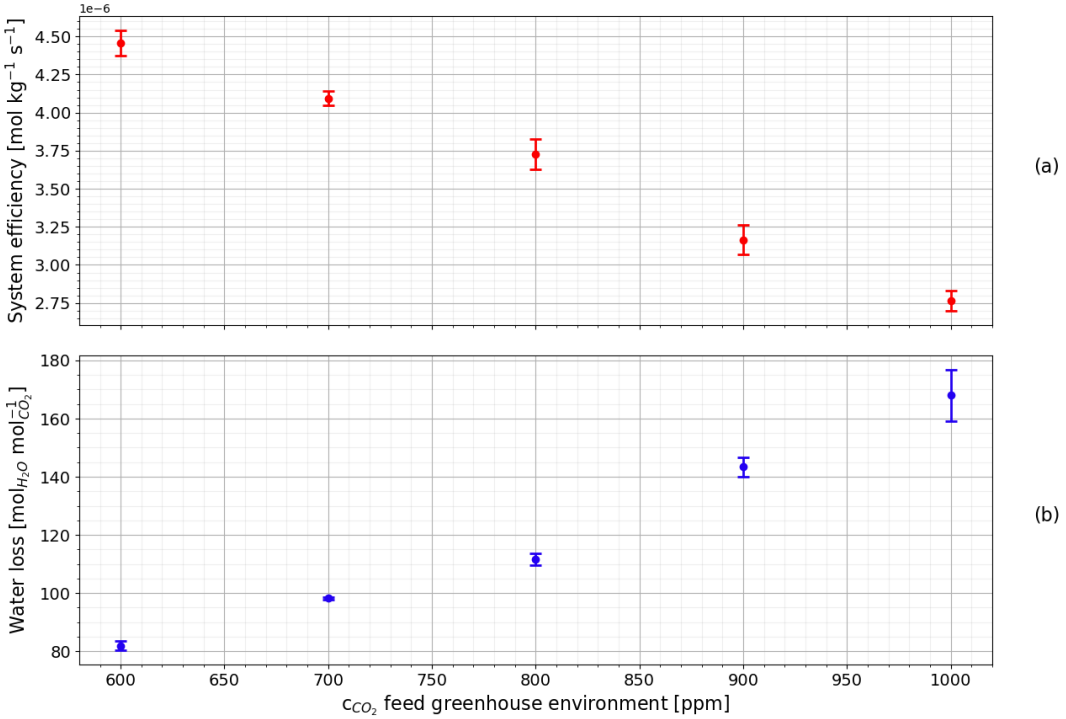

Figure 5.12: Mean system efficiency and water loss of the adsorption-desorption cycle for different CO_2 concentrations inside the greenhouse, including the error.

5.2.4. Limits Controlling the System

To optimize the adsorption process in the column, a controlling system has been designed. This control system changes the gas flowing through the column, transitioning from atmospheric air to greenhouse air and initiating desorption of CO_2 before complete saturation occurs. Operational limits are set, based on the CO_2 concentration at the outflow. Specifically, during the adsorption phase, when the outflow CO_2 concentration reaches 99% of the inlet feed concentration, the system switches to greenhouse air. Conversely, during the desorption phase, when the outflow concentration equals 101% of the feed concentration, the system switches back to atmospheric air. These limits dictate the duration of a single adsorption-desorption cycle and the quantity of CO_2 that can be adsorbed and released in the greenhouse environment within one cycle. Importantly, these limits are expressed as a percentage of the feed concentration at the inlet, which varies between greenhouse air and atmospheric air.

Switching limits (e.g., breakthrough point) determine the cycle's efficiency. If the switch occurs too late, the column's efficiency decreases due to saturation. If too early, potential adsorption capacity is wasted. If switched too late, more water might be adsorbed with CO2, increasing water loss during desorption.

Figure 5.13a illustrates the system efficiency, while Figure 5.13b depicts the water loss for various

limits of outflow concentration during the adsorption phase. Notably, the results remain relatively stable across different limits, except when the outflow concentration exceeds 95% of the inlet concentration, leading to a significant decrease in the system efficiency and an increase in the water loss. The lower limits between 80% and 88% are unexpected and random. Decreasing this limit would mean, the system switches at an earlier stage from adsorption to desorption, decreasing the cycle time and also wasting potential adsorption capacity. The water loss due an increased number of switches should become dominant and eventually increase the water loss for lower limits. The current results show lower limits are preferred despite the increased frequency of switches, as they result in reduced overall water loss while maintaining near-constant efficiency.

Figure 5.14 shows respectively the system efficiency and the water loss for different limits of the outflow concentration during the desorption phase. Setting the outflow gas concentration limit below 108% of the inlet gas concentration significantly reduces the system efficiency and increases the water loss. Compared to the adsorption limit, the desorption limit shows more what we expected and shows an optimum limit between 102% and 104%. Interesting is the difference in curve between the adsorption and desorption limit, this is caused due to the faster desorption kinetics. The desorption time is lower compared to the adsorption time, together with a lower feed concentration, the optimum limit is reached at a lower percentage. The results show larger errors, this is caused due to the time steps of the solver. The concentration profiles become during the desorption step are linear and the solver increases the time steps, causing the system to switch depending on the time steps to switch later and so create different cycle times. The desorption limit has an optimum, which gives the minimum amount of water loss and a maximum system efficiency.

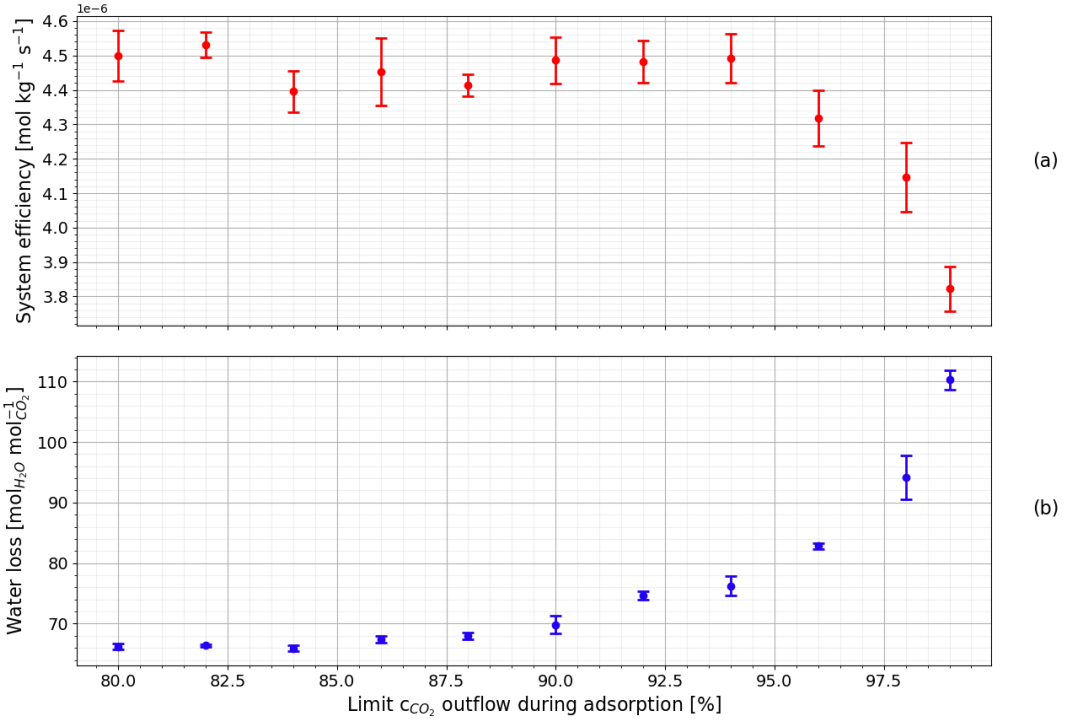

Figure 5.13: Mean system efficiency and water loss of the adsorption-desorption cycle for different adsorption threshold values, including the error.

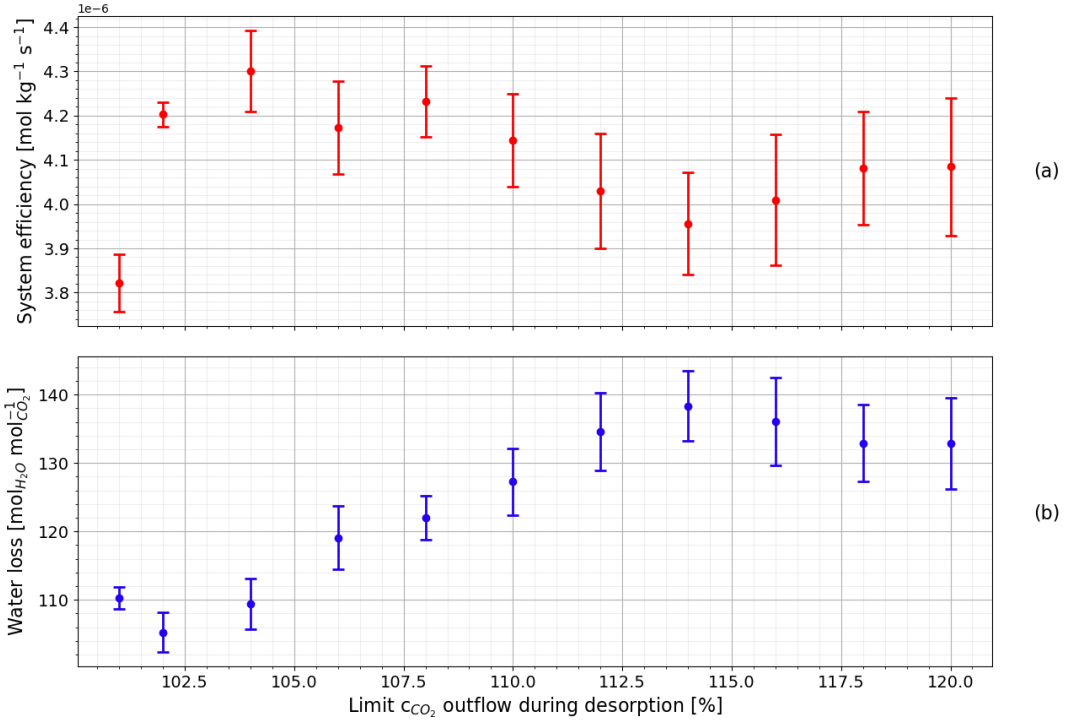

Figure 5.14: Mean system efficiency and water loss of the adsorption-desorption cycle for different desorption threshold values, including the error.

6

Techno-Economic Viability Analysis

6.1. Capital Expenditures

The shape of the column determines not only the potential capacity of the system, the efficiency, and the water loss. It also is a factor that determines the CAPEX, and depending on the costs the trade-off can be made to make just one larger column or several smaller columns. First the effect of the length in combination with the velocity is shown in Figure 6.1. As expected increasing the length or the superficial velocity increases the pressure drop through the column. The second observation is when the bed length increases, the effect of the velocity on the pressure drop increases. A larger column would decrease the efficiency, to increase the efficiency the velocity must be increased, which mean the pressure drop of a larger column is significant higher compared to a smaller column with the same efficiency.

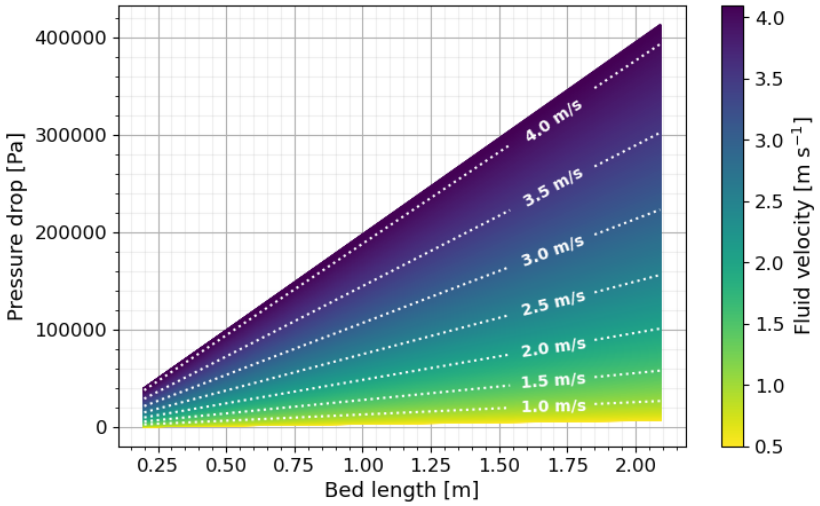

Figure 6.1: Pressure drop through the column related to the bed length and the superficial velocity according to the Ergun equation.

The effect of the length of the column on the CAPEX is shown in Figure 6.2. Increasing the length increases the costs for the internal components and the shell costs. The fan and auxiliary costs are in this configuration much smaller compared to the other costs. Several smaller costs relatively more compared to a large column, except the efficiency of smaller columns is higher according to Chapter 5. On the long term this means a smaller adsorption column becomes interesting, while on short terms a longer adsorption column is beneficial.

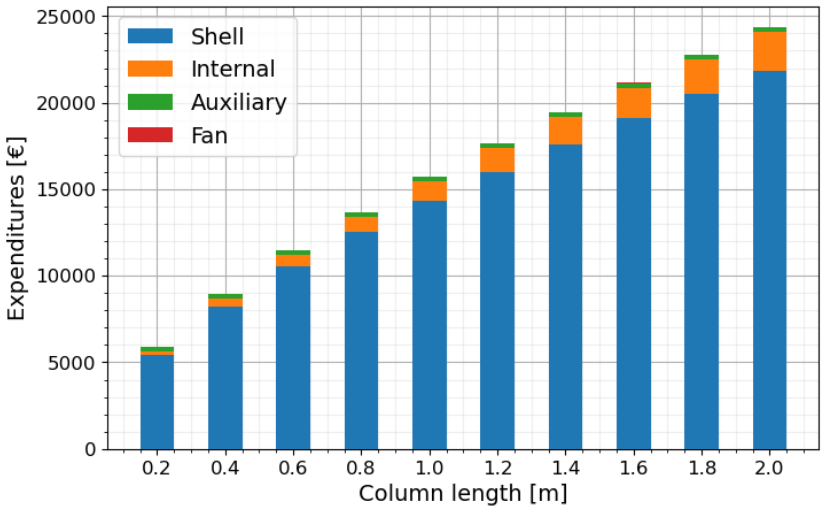

Figure 6.2: Capital expenditures of the base perspective adsorption column for different column lengths, including the shell costs, internal component costs, auxiliary costs, and the fan costs.

Figure 6.3 shows the CAPEX of the base perspective design for different diameters. The increase in diameter shows an significant increase in internal costs, this is due to the increased volume of the column. The column volume increases with the squared diameter of the column, while the shell volume increases with the diameter of the column.

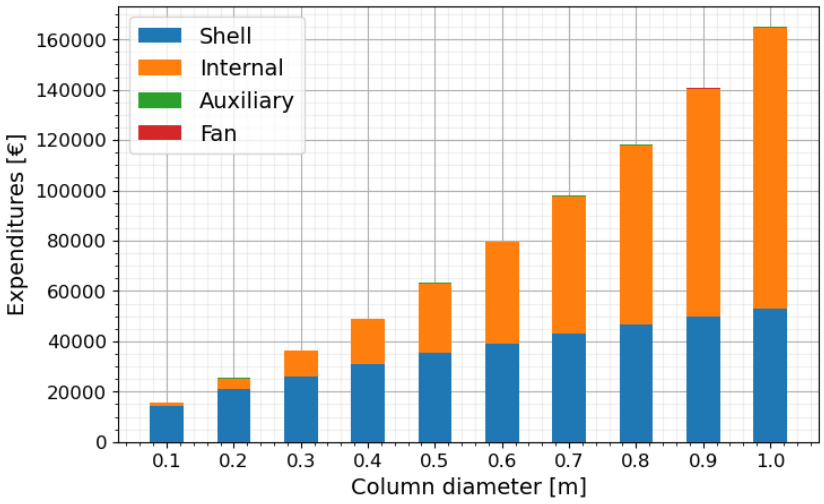

Figure 6.3: Capital expenditures of the base perspective adsorption column for different column diameters, including the shell costs, internal component costs, auxiliary costs, and the fan costs.

The velocity will only affect the fan costs, which in this base perspective negligible compared to the shell costs. Figure 6.4 shows a slight increase in fan costs with increasing the velocity. Increasing the velocity has not a significant effect on the CAPEX, while it significantly increases the efficiency of the sorbent, but also increases the water consumption.

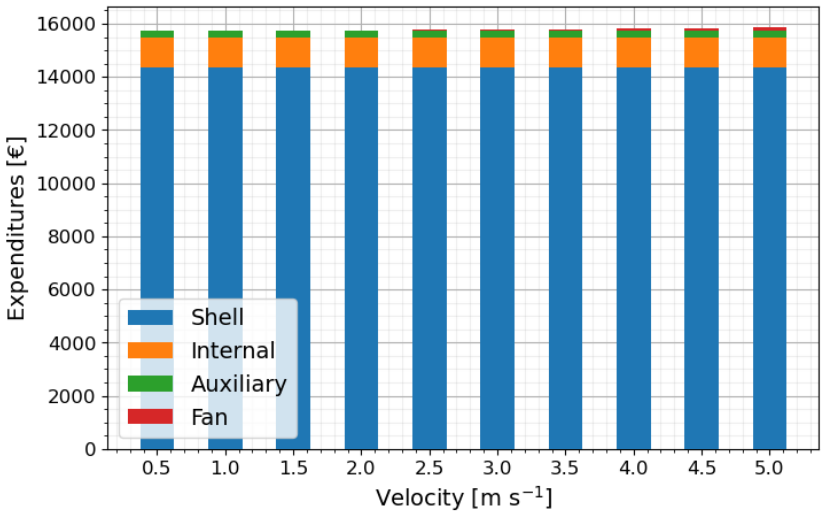

Figure 6.4: Capital expenditures of the base perspective adsorption column for different column lengths, including the shell costs, internal component costs, auxiliary costs, and the fan costs.

Last, the effect of the total length of external pipes necessary for the system is shown in Figure 6.5. Increasing the total pipe length causes the auxiliary costs to go up and making them not negligible anymore.

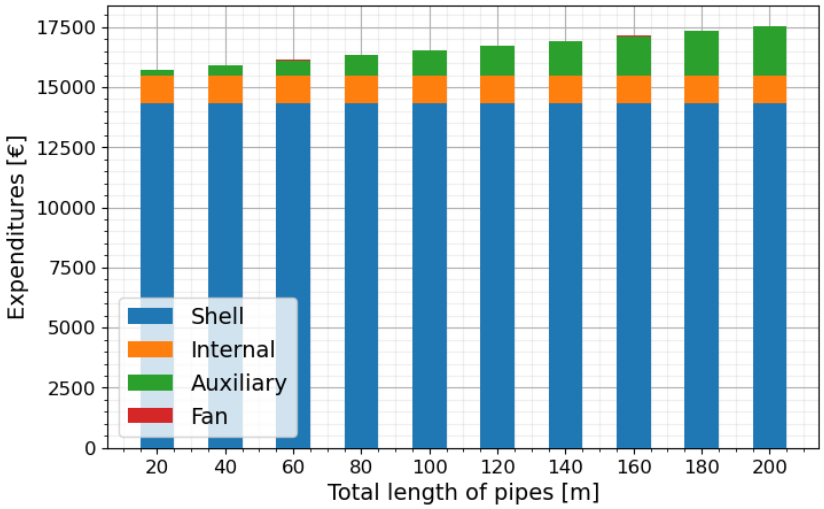

Figure 6.5: Capital expenditures of the base perspective adsorption column for total lengths of external pipes, including the shell costs, internal component costs, auxiliary costs, and the fan costs.

6.2. Operating Expenditures

The water loss in the sensitivity analysis of Chapter 5 showed variations between 50 and 700 moles of water per mole CO_2 moved to the greenhouse. The tap water price was assumed around €5 per cubic meter water, and an irrigation water price of €0.65 per cubic meter water. Figure 6.6 shows the costs per mole of adsorbed CO_2 according to the water loss range from the sensitivity analysis. Assuming the highest water loss, to reach the 100 to 200 kilogram per hectare per hour that is required to keep a CO_2 concentration level of 1000 ppm, the irrigation water costs are €18.77 to €37.53 per hectare per hour. If tap water would be used the costs would increase to €143.59 to €287.18 per hectare per hour. This are maximum prices, according to the results in Chapter 5 the water loss can be reduced by optimizing the system which will significantly decrease the costs of water according to these results, making it an interesting option from the water costs point of view.

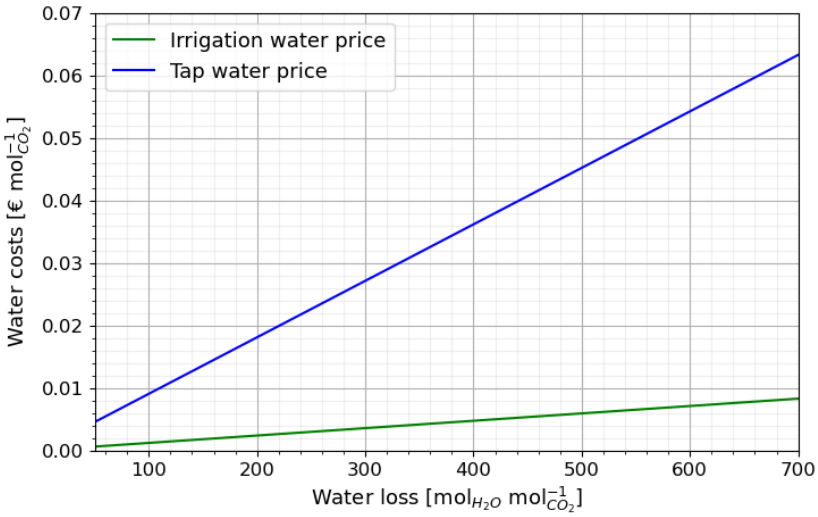

Figure 6.6: Operating expenditures of water per mole of adsorbed CO_2 according to the water loss of the system.

The electricity price was assumed to be 0.5 US dollars per kilowatt-hour, which is equal to €0.46 per kilowatt-hour. vary a lot between countries, from 0.008 to 0.585 US dollars per kilowatt-hour, as shown in Figure 3.5. The variation is caused by the geographical location and makeup of a country, level of development, and the economy. Assuming the base perspective with a system productivity of 90.07 micromoles of CO_2 per second. To meet the required greenhouse input of 0.5 moles per second to maintain a concentration of 1000 ppm, 5551 adsorption columns of the base perspective are required. So, there are 5551 fans necessary for a productivity of 0.5 moles per second per hectare, equal to 1800 moles per hour. The required fan power is 0.38 kW, thus during a hour a total of 2109.38 kWh is required, equal to 1.17 kWh per mole of CO_2. The electricity costs of the base perspective are €0.54 per mole of CO_2, which is equal to €972 per hectare per hour. So, the electricity costs are larger compared to the water costs.

Figure 6.7a shows the effect of the velocity and the column length on the required fan power. For lower velocity the length of the column has less effect compared to higher velocities. Figure 6.7b shows the effect of the velocity and the diameter of the column on the required fan power. Comparable to the column length, the diameter has less effect on the fan power at lower velocities. The difference between the column length, where the fan power increases linear, the fan power increases the exponential with the column diameter. This observation occurs due to the increasing of the flow area of the column with the square of the diameter, which causes the pressure drop to increase with the same factor.

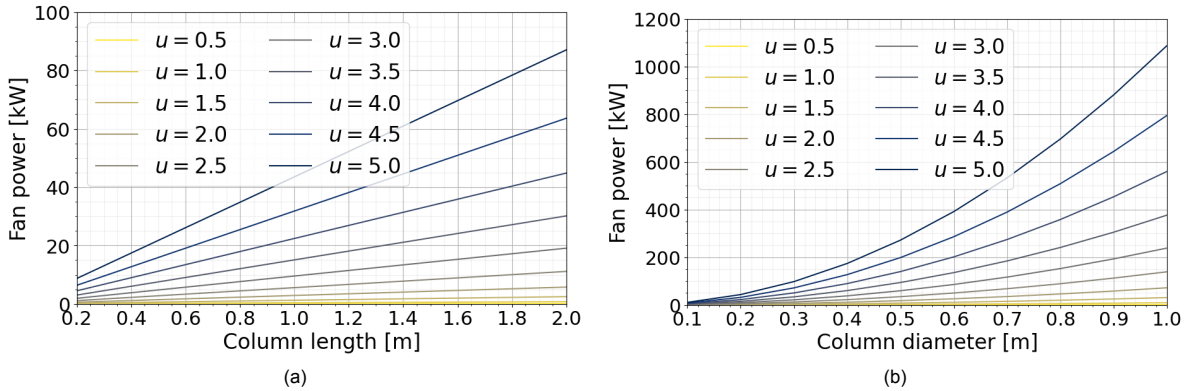

(a) (b)

Figure 6.7: (a) The fan power of an adsorption column with a length of 1 meter, for different column lengths (a) and for different column diameters (b).

7

Conclusion and Recommendations

The performance, climatic adaptability, and the economic viability of a moisture swing system to capture CO_2 from the air and utilize it in a greenhouse is analyzed through a combination of literature review, data analysis, and numerical modelling. The conclusions are drawn in the answers to the five sub-questions, and ultimately answering the main research question.

What are the key parameters impacting the feasibility and efficiency of the system?
The key parameters impacting the feasibility and efficiency of the system include relative humidity, temperature, and CO□ concentration in the gas phase. The primary key parameter affecting the saturation coverage of the moisture swing sorbent is the relative humidity. Changes in relative humidity showed higher saturation differences compared to a change in temperature or CO_2 concentration of the air. To use the full potential of the sorbent, the difference between the saturation coverage during the adsorption stage and the desorption stage must be large. A relative humidity lower than 0.4 during adsorption resulted in reaching 0.9 to 1.0 saturation coverage, and the effects of the temperature and the CO_2 concentration became minimal. For an optimal performance of the sorbent, a low humidity (below 0.5), a low temperature (below 20°C), and a high CO_2 concentration (400 to 1000 ppm) are preferred during the adsorption stage. Conversely, a high humidity (0.6 to 1.0), a high temperature (above 10°C), and a low CO_2 concentration (200 to 400 ppm) are preferred during the desorption stage.

How does the moisture swing sorbent perform under various climatic conditions worldwide, considering specific combinations of humidity, and temperature?
The three key parameters are all climatic conditions of the atmospheric air, which are related to the geographical location and the time. The literature study showed the interesting climate classes according to the key parameters are especially the arid climates around the Sahara, southern Africa, Australia, and the Middle East. The seasonal results confirmed this observation, where the highest 5-year mean saturation coverage was reached in regions like the Sahara, the Middle East, southern Africa, and Australia, but also western United States, Chile, and Central Asia. The seasonal and diurnal deviations were lower in these regions with higher mean saturation coverages, ensuring a stable performance. Regions with distinct seasons, like monsoon areas, exhibited higher seasonal deviations. The change from day to night showed the most decrease in regions around the equator with a tropical climate, like Brazil and Central Africa. Together with the more specific country and city results can be concluded that the most suitable locations to achieve the full potential of the capacity of the sorbent are the arid countries in mainly Africa and Asia, like Algeria, Niger, Saudi-Arabia, and Kuwait for example. Those countries reach mean saturation coverages up to 0.940 with small deviations. In the other continents, like Europe, the largest mean saturation coverages are between 0.72 and 0.73 in countries like Moldavia, Albania, and Greece. So, the most promising regions are in Africa and Asia, but if the inside air conditions of the greenhouse are optimal a moisture swing sorbent could become interesting in other continents.

How do the parameters and conditions affect the performance of the moisture swing DAC system in a closed greenhouse environment?
The sensitivity analysis of the design parameters and the atmospheric air and greenhouse conditions resulted in a clear insight in their effects on the performance of the system. By investigation of realistic parameters and conditions, a first indication of the potential of the system has been made.

The length of the column had an effect on the efficiency, the water loss, and the productivity of the system. A larger column had a negative effect on the efficiency of the sorbent, but a positive effect on the water loss and the productivity. So, a larger column decreases the number of columns needed to satisfy the greenhouse requirements of 0.5 to 1.0 moles of CO_2 per second per hectare. The diameter of the column only affect the productivity of the system, and the required fan power. Increasing the diameter is beneficial for the productivity of the system, which decreases the number of required columns for a greenhouse. However, this also increases the power of the fan to reach the required superficial velocity. A smaller column is most efficient, however, a larger column will be necessary to reduce the number of columns required.

The relative humidity of the air passing through the column was another important factor. The model of the system was most efficient and experiences minimal water loss with low outside humidities. Therefore, the design should focus on achieving the lowest possible relative humidity for the atmospheric air entering the system. Conversely, inside the greenhouse, maintaining a high humidity is needed to support the moisture adsorption process. However, there are limitations on the humidities. Outside the greenhouse, the humidity depends on the climate and the geographical location. Most regions do not achieve humidities lower than 0.5, only the regions with an arid climate achieve lower humidities. Inside the greenhouse, the humidity is limited by the crop requirements, most greenhouses operate between humidities of 60 to 85%. Thus, optimizing the system involves a low outside humidity and a high inside humidity, as expected from the isotherm of the sorbent.

Temperature plays a minor role in the performance of the moisture adsorption process compared to humidity levels. The system should aim for a low outside temperature while maintaining a high inside temperature in the greenhouse to maximize adsorption efficiency and minimize water loss. However, a higher temperature difference leads to increased heat losses, necessitating more thermal energy to maintain the desired greenhouse temperature. Therefore, the goal became to minimize internal heating load, maximize system efficiency, and reduce water loss, all while considering crop-specific temperature requirements. Additionally, outside temperatures depends on the regional climate, with arid climates typically experiencing higher temperatures.

The concentration of CO_2 fed into the system from inside the greenhouse during desorption had a minor effect compared to the humidity. To maintain the efficiency of the moisture adsorption process and reduce overall water loss, the feed concentration during desorption should be kept as low as possible. However, most crops require a higher CO_2 concentration inside the greenhouse to increase crop yield. Therefore, the CO_2 concentration inside the greenhouse should be kept as low as possible, while still meeting the desired concentration for crop growth.

The switch thresholds determined the moments the model switches from adsorption to desorption, and vice versa. Switching too late decreased the efficiency of the column and increased the water loss, while switching to early wasted potential adsorption capacity of the sorbent and also resulted also in a lower efficiency and more water loss. Setting the adsorption threshold to 92 to 98% of the feed concentration resulted in more switches but increases efficiency and decreases water loss. Raising the desorption limit initially increases efficiency but eventually leads to an decrease. The desorption limit showed optimal water loss at 102% of the feed concentration and optimal efficiency at 104%. Therefore, there is a clear optimal desorption limit, but no optimal adsorption limit was determined, likely due to inaccuracies in the solving method.

Four configuration are proposed based on the sensitivity analysis of the parameters and conditions to improve the efficiency, the productivity and the water loss. This resulted in a first indication of the performance potential of a moisture swing DAC system in a greenhouse. Table 7.1 shows the parameter and performance results of the four configuration, all configurations had enhanced efficiency, water loss, and productivity compared to the base perspective. To meet a greenhouse's CO_2 requirement of 0.5 moles per hectare per second, options include: 2035 small columns at lower velocity (C.1), 1470

small columns at higher velocity (C.2), 84 larger columns at lower velocity (C.3), or 53 larger columns at higher velocity (C.4). Due to the high number of columns needed, implementing larger columns is advisable to reduce their quantity while decreasing sorbent efficiency.

Table 7.1: Design parameters and performance results of four different configuration designs, with an outside relative humidity and temperature of 0.45 and 18°C, an inside relative humidity and temperature of 0.75 and 26°C, an inside CO_2 concentration of 700 ppm, an adsorption outflow threshold limit of 94%, and a desorption outflow threshold limit of 102%.

Property	Unit	C.1	C.2	C.3	C.4
Column length L_{bed}	m	0.6	0.6	1.6	1.6
Column diameter d_{bed}	m	0.2	0.2	0.8	0.8
Gas velocity u	$m \cdot s^{-1}$	2.0	4.0	2.0	4.0
System efficiency η	$\mu mol \cdot kg^{-1} \cdot s^{-1}$	17.4	24.1	9.9	15.0
System water loss n_{loss}	$mol_{H_2O} \cdot mol_{CO_2}^{-1}$	50.4	65.3	36.4	45.4
System productivity $\dot{m}_{prod}$	$mmol \cdot s^{-1}$	0.246	0.340	5.957	9.051

How do water availability and energy costs around different places in the world influence the economic feasibility of moisture swing DAC for CO_2 enrichment in greenhouses?
In the short term, the CAPEX dominates the system costs, with initial costs for moisture swing adsorption columns being high, even for smaller columns. Therefore, increasing the column size is advantageous from a CAPEX perspective, as it reduces the overall number of columns required per greenhouse. Looking ahead to the long term, assuming potential reductions in CAPEX due to lower material costs and possible sustainability fairs, the OPEX becomes important. The electricity costs, according to our base perspective, constitute the largest component compared to water costs. However, the challenge lies in assessing the right economic value of water, which varies depending on geographical location, demand, availability, and water quality. The OPEX estimation presented here provides a simplified overview of costs. A comprehensive techno-economic analysis is essential to compare the costs to an alternative sustainable solution. Such an analysis requires an extensive optimization of the system, as the current results offered only preliminary insights into feasibility and efficiency.

What challenges exist for further practical implementation of moisture swing DAC systems in closed greenhouse environments?
As previously discussed, this is a first investigation of the feasibility and efficiency of implementing a moisture swing system for CO_2 enrichment in a closed greenhouse environment. While he performance results are not optimal, it remains a sustainable innovation that can be a valuable solution in specific cases. The next step involves optimizing the system parameters to maximize efficiency and productivity, and minimize water loss. It is expected multiple configurations will become interesting, each balancing trade-offs between a high efficiency with a higher water loss versus a lower water loss with a reduced efficiency. A multi-objective optimization approach, such as a Pareto front approach, will be essential to explore these trade-offs comprehensively. Following optimization, an extensive techno-economic analysis will be necessary to compare the moisture swing system against alternative sustainable solutions, like a thermal swing adsorption systems using a heat pump. Eventually, further experimental studies are necessary to validate the performance of optimized system designs in real-world greenhouse operations. Practical challenges are identified as the need for enhanced sorbents with higher CO_2 capture capacities and faster kinetics, integrating renewable energy sources to reduce operational costs, and ensuring a sustainable water source. Initially focusing on optimizing system performance will create a path to experimental implementations in greenhouse settings.

What are the feasibility and efficiency of implementing a moisture-swing DAC system for CO_2 enrichment in a closed greenhouse environment for optimized plant growth and productivity?
The results showed a moisture-swing DAC system can potentially be an interesting innovation to a greenhouse. The current configurations of the adsorption column analyzed resulted in a large amount of necessary columns to achieve the required amount of CO_2 in a greenhouse. Nevertheless, the solution of a system with as driving force a difference in humidities is a very interesting solution from the economical view if the costs of the sorbent can be reduced and the capacity of the sorbent could be improved. And even with the current capacity, a more extensive multi-objective optimization analysis is expected to improve the system and results in less amount of columns necessary.

Bibliography

[1] IPCC, “Climate Change 2014: Synthesis Report. Contribution of Working Groups I, II and III to the Fifth Assessment Report of the Intergovernmental Panel on Climate Change,” R. P. Core Writing Team and L. M. (eds.), Eds., p. 151, 2014. [Online]. Available: https://www.ipcc.ch/site/assets/uploads/2018/02/SYR_AR5_FINAL_full.pdf.

[2] Y. Malhi, J. Franklin, N. Seddon, *et al.*, “Climate change and ecosystems: Threats, opportunities and solutions,” *Philosophical Transactions of the Royal Society B*, vol. 375, no. 1794, p. 20 190 104, 2020. DOI: 10.1098/rstb.2019.0104.

[3] O. Hoegh-Guldberg and J. F. Bruno, “The impact of climate change on the world’s marine ecosystems,” *Science*, vol. 328, no. 5985, pp. 1523–1528, 2010. DOI: 10.1126/science.1189930.

[4] National Centers for Environmental Information, *Global temperature anomalies*, 2023. [Online]. Available: https://www.ncei.noaa.gov/access/monitoring/global-temperature-anomalies/anomalies.

[5] Global Carbon Project - with major processing by Our World in Data, *Total (fossil fuels and land-use change)* – GCB, Global Carbon Project, 2023. [Online]. Available: https://www.globalcarbonproject.org/carbonbudget/archive.htm.

[6] UNFCCC, *The paris agreement*, 2015. [Online]. Available: https://unfccc.int/process-and-meetings/the-paris-agreement.

[7] M. L. Parry, T. R. Carter, and N. T. Konijn, *The Impact of Climatic Variations on Agriculture, Volume 1: Assessment in Cool Temperate and Cold Regions*. Springer Dordrecht, 1988, p. 888. doi: 10.1007/978-94-009-2943-2.

[8] H. Eswaran, E. Van Den Berg, and P. Reich, “Organic Carbon in Soils of the World,” *Soil Science Society of America Journal*, vol. 57, no. 1, pp. 192–194, 1993. doi: 10.2136/sssaj1993.03615995005700010034x.

[9] S. Sinha and M. Swaminathan, “Deforestation, climate change and sustainable nutrition security: A case study of india,” *Climatic Change*, vol. 19, no. 1-2, pp. 201–209, 1991. doi: 10.1007/BF00142227.

[10] G. D. Rao and S. Sinha, “Impact of climate change on simulated wheat production in india,” *Implications of climate change for international agriculture: crop modelling study*, vol. 2, no. 3, pp. 4–, 1994.

[11] T. E. Downing, “The effects of climate change on agriculture and food security,” *Renewable Energy*, vol. 3, no. 4-5, pp. 491–497, 1993. doi: 10.1016/0960-1481(93)90115-W.

[12] N. D. Mueller, P. C. West, J. S. Gerber, G. K. MacDonald, S. Polasky, and J. A. Foley, “A tradeoff frontier for global nitrogen use and cereal production,” *Environmental Research Letters*, vol. 9, no. 5, p. 054 002, 2014.

[13] Z. Chalabi, A. Biro, B. Bailey, D. Aikman, and K. Cockshull, “Erratum-optimal control strategies for carbon dioxide enrichment in greenhouse tomato crops part 1: Using pure carbon dioxide [biosystems engineering (2002) 81 (4), 421-431],” *Biosystems Engineering*, vol. 1, no. 83, p. 127, 2002. doi: 10.1006/bioe.2001.0108.

[14] D. Willits and M. Peet, “Predicting yield responses to different greenhouse co2 enrichment schemes: Cucumbers and tomatoes,” *Agricultural and Forest Meteorology*, vol. 44, no. 3-4, pp. 275–293, 1989. doi: 10.1016/0168-1923(89)90022-1.

[15] B. Tisserat, S. F. Vaughn, and M. A. Berhow, “Ultrahigh co2 levels enhances cuphea growth and morphogenesis,” *industrial crops and products*, vol. 27, no. 1, pp. 133–135, 2008. doi: 10.1016/j.indcrop.2007.06.003.

[16] E. Nederhoff and C. Stanghellini, *Water use efficiency of tomatoes. practical hydroponics and greenhouses,(115): 52-59*, 2010.

[17] J. Bao, W.-H. Lu, J. Zhao, and X. T. Bi, “Greenhouses for co2 sequestration from atmosphere,” *Carbon Resources Conversion*, vol. 1, no. 2, pp. 183–190, 2018. doi: 10.1016/j.crcon.2018.08.002.

[18] D. H. Jung, I. Hwang, and J. E. Son, “Three-dimensional estimation of greenhouse-grown mango photosynthesis with different co2 enrichment heights,” *Horticulture, Environment, and Biotechnology*, vol. 63, no. 6, pp. 823–834, 2022. doi: 10.1007/s13580-022-00453-3.

[19] Y. Zhang, D. Yasutake, K. Hidaka, T. Okayasu, M. Kitano, and T. Hirota, “Crop-localised co2 enrichment improves the microclimate, photosynthetic distribution and energy utilisation efficiency in a greenhouse,” *Journal of Cleaner Production*, vol. 371, p. 133 465, 2022. doi: 10.1016/j.jclepro.2022.133465.

[20] L. M. Mortensen, “Co2 enrichment in greenhouses. crop responses,” *Scientia Horticulturae*, vol. 33, no. 1-2, pp. 1–25, 1987. doi: 10.1016/0304-4238(87)90028-8.

[21] S. Zhang, X. T. Bi, and R. Clift, “A life cycle assessment of integrated dairy farm-greenhouse systems in british columbia,” *Bioresource technology*, vol. 150, pp. 496–505, 2013. doi: 10.1016/j.biortech.2013.09.076.

[22] A. Wang, J. Lv, J. Wang, and K. Shi, “Co2 enrichment in greenhouse production: Towards a sustainable approach,” *Frontiers in Plant Science*, vol. 13, p. 1 029 901, 2022. doi: 10.3389/fpls.2022.1029901.

[23] U. Pérez-López, J. Miranda-Apodaca, M. Lacuesta, A. Mena-Petite, and A. Muñoz-Rueda, “Growth and nutritional quality improvement in two differently pigmented lettuce cultivars grown under elevated co2 and/or salinity,” *Scientia Horticulturae*, vol. 195, pp. 56–66, 2015. doi: 10.1016/j.scienta.2015.08.034.

[24] P. Vermeulen, “Alternative sources of co2 for the greenhouse horticulture,” in *Proceedings of the 2nd International Symposium on Energy Challenges and Mechanics (ECM2), Aberdeen, UK*, 2014, pp. 19–21.

[25] L.-M. Dion, M. Lefsrud, and V. Orsat, “Review of co2 recovery methods from the exhaust gas of biomass heating systems for safe enrichment in greenhouses,” *Biomass and bioenergy*, vol. 35, no. 8, pp. 3422–3432, 2011. doi: 10.1016/j.biombioe.2011.06.013.

[26] B. Marchi, S. Zanoni, and M. Pasetti, “Industrial symbiosis for greener horticulture practices: The co2 enrichment from energy intensive industrial processes,” *Procedia CIRP*, vol. 69, pp. 562–567, 2018. doi: 10.1016/j.procir.2017.11.117.

[27] A. M. Syed and C. Hachem, “Review of design trends in lighting, environmental controls, carbon dioxide supplementation, passive design, and renewable energy systems for agricultural greenhouses,” *Journal of Biosystems Engineering*, vol. 44, pp. 28–36, 2019. doi: 10.1007/s42853-019-00006-0.

[28] M. Poudel and B. Dunn, “Greenhouse carbon dioxide supplementation,” Oklahoma Cooperative Extension Service, Tech. Rep., 2017.

[29] Q. Sun *et al.*, “Impact of illumination and temperature performance of blanket-inside solar greenhouse and co2 enrichment on cucumber growth and development,” *Agricultural Science & Technology*, vol. 17, no. 8, p. 1757, 2016. doi: 10.16175/j.cnki.1009-4229.2016.08.001.

[30] M. F. Karim *et al.*, “Effects of co2 enrichment by fermentation of cram on growth, yield and physiological traits of cherry tomato,” *Saudi Journal of Biological Sciences*, vol. 27, no. 4, p. 1041, 2020. doi: 10.1016/j.sjbs.2020.02.020.

[31] Y. Li, Y. Ding, D. Li, and Z. Miao, “Automatic carbon dioxide enrichment strategies in the greenhouse: A review,” *Biosystems engineering*, vol. 171, pp. 101–119, 2018. doi: 10.1016/j.biosystemseng.2018.04.018.

[32] C. Tang *et al.*, “Investigation on the rotary regenerative adsorption wheel in a new strategy for co2 enrichment in greenhouse,” *Applied Thermal Engineering*, vol. 205, p. 118 043, 2022. doi: 10.1016/j.applthermaleng.2022.118043.

[33] T. Wang, J. Huang, X. He, J. Wu, M. Fang, and J. Cheng, “Co2 fertilization system integrated with a low-cost direct air capture technology,” *Energy Procedia*, vol. 63, pp. 6842–6851, 2014. doi: 10.1016/j.egypro.2014.11.718.

[34] L. Jiang *et al.*, “Sorption direct air capture with co2 utilization,” *Progress in Energy and Combustion Science*, vol. 95, p. 101 069, 2023. doi: 10.1016/j.pecs.2022.101069.

[35] J. Sun, M. Zhao, L. Huang, T. Zhang, and Q. Wang, “Recent progress on direct air capture of carbon dioxide,” *Current Opinion in Green and Sustainable Chemistry*, p. 100 752, 2023. doi: 10.1016/j.cogsc.2023.100752.

[36] A. Sodiq *et al.*, “A review on progress made in direct air capture of co2,” *Environmental Technology & Innovation*, p. 102 991, 2022. doi: 10.1016/j.eti.2022.102991.

[37] X. Zhu, S. Li, Y. Shi, and N. Cai, “Recent advances in elevated-temperature pressure swing adsorption for carbon capture and hydrogen production,” *Progress in Energy and Combustion Science*, vol. 75, p. 100 784, 2019. doi: 10.1016/j.pecs.2019.100784.

[38] S. Fujikawa and R. Selyanchyn, “Direct air capture by membranes,” *MRS Bulletin*, vol. 47, no. 4, pp. 416–423, 2022. doi: 10.1557/s43577-022-00313-6.

[39] C. Chao, Y. Deng, R. Dewil, J. Baeyens, and X. Fan, “Post-combustion carbon capture,” *Renewable and Sustainable Energy Reviews*, vol. 138, p. 110 490, 2021. doi: 10.1016/j.rser.2020.110490.

[40] J. Ling, A. Ntiamoah, P. Xiao, P. A. Webley, and Y. Zhai, “Effects of feed gas concentration, temperature and process parameters on vacuum swing adsorption performance for co2 capture,” *Chemical Engineering Journal*, vol. 265, pp. 47–57, 2015. doi: 10.1016/j.cej.2014.11.121.

[41] L. Jiang, A. Roskilly, and R. Wang, “Performance exploration of temperature swing adsorption technology for carbon dioxide capture,” *Energy Conversion and Management*, vol. 165, pp. 396–404, 2018. doi: 10.1016/j.enconman.2018.03.077.

[42] S. M. Wilson and F. H. Tezel, “Direct dry air capture of co2 using vtsa with faujasite zeolites,” *Industrial & Engineering Chemistry Research*, vol. 59, no. 18, pp. 8783–8794, 2020. doi: 10.1021/acs.iecr.9b04803.

[43] M. Fasihi, O. Efimova, and C. Breyer, “Techno-economic assessment of co2 direct air capture plants,” *Journal of cleaner production*, vol. 224, pp. 957–980, 2019. doi: 10.1016/j.jclepro.2019.03.086.

[44] A. R. Cuesta and C. Song, “Ph swing adsorption process for ambient carbon dioxide capture using activated carbon black adsorbents and immobilized carbonic anhydrase biocatalysts,” *Applied Energy*, vol. 280, p. 116 003, 2020. doi: 10.1016/j.apenergy.2020.116003.

[45] X. Duan *et al.*, “Chemisorption and regeneration of amine-based co2 sorbents in direct air capture,” *Materials Today Sustainability*, vol. 23, p. 100 453, 2023. doi: 10.1016/j.mtsust.2023.100453.

[46] H. Barbour *et al.*, “The commercial case for direct air capture,” 2021.

[47] M. Ozkan, S. P. Nayak, A. D. Ruiz, and W. Jiang, “Current status and pillars of direct air capture technologies,” *Iscience*, 2022. doi: 10.1016/j.isci.2022.103990.

[48] X. Shi, H. Xiao, K. Kanamori, A. Yonezu, K. S. Lackner, and X. Chen, “Moisture-driven co2 sorbents,” *Joule*, vol. 4, no. 8, pp. 1823–1837, 2020. doi: 10.1016/j.joule.2020.07.005.

[49] T. Wang, K. S. Lackner, and A. Wright, “Moisture swing sorbent for carbon dioxide capture from ambient air,” *Environmental science & technology*, vol. 45, no. 15, pp. 6670–6675, 2011. doi: 10.1021/es201180v.

[50] SnowPure Water Technologies, *Excellmembranes*, Excellion Ion Exchange Membranes Specification Sheet, 2018. [Online]. Available: https://www.snowpure.com/wp-content/uploads/2018/08/Excellion-Specifications-2018a.pdf.

[51] H. He *et al.*, “Carbon black functionalized with hyperbranched polymers: Synthesis, characterization, and application in reversible co 2 capture,” *Journal of Materials Chemistry A*, vol. 1, no. 23, pp. 6810–6821, 2013. doi: 10.1039/c3ta10699c.

[52] H. He *et al.*, “Three-dimensionally ordered macroporous polymeric materials by colloidal crystal templating for reversible co2 capture,” *Advanced Functional Materials*, vol. 23, no. 37, pp. 4720–4728, 2013. doi: 10.1002/adfm.201300401.

[53] H. He *et al.*, “Porous polymers prepared via high internal phase emulsion polymerization for reversible co2 capture,” *Polymer*, vol. 55, no. 1, pp. 385–394, 2014. doi: 10.1016/j.polymer.2013.08.002.

[54] T. Wang, J. Liu, H. Huang, M. Fang, and Z. Luo, “Preparation and kinetics of a heterogeneous sorbent for co2 capture from the atmosphere,” *Chemical Engineering Journal*, vol. 284, pp. 679–686, 2016. doi: 10.1016/j.cej.2015.09.009.

[55] X. Shi, Q. Li, T. Wang, and K. S. Lackner, “Kinetic analysis of an anion exchange absorbent for co2 capture from ambient air,” *PLoS One*, vol. 12, no. 6, e0179828, 2017. doi: 10.1371/journal.pone.0179828.

[56] C. Hou, Y. Wu, T. Wang, X. Wang, and X. Gao, “Preparation of quaternized bamboo cellulose and its implication in direct air capture of co2,” *Energy & Fuels*, vol. 33, no. 3, pp. 1745–1752, 2018. doi: 10.1021/acs.energyfuels.8b02821.

[57] J. Song *et al.*, “Quaternized chitosan/pva aerogels for reversible co2 capture from ambient air,” *Industrial & Engineering Chemistry Research*, vol. 57, no. 14, pp. 4941–4948, 2018. doi: 10.1021/acs.energyfuels.8b02821.

[58] D. Molden, *Water for food water for life: A comprehensive assessment of water management in agriculture*. Routledge, 2013.

[59] Our World in Data, *Water withdrawals and consumption - aquastat*, Processed by Our World in Data, 2015.

[60] M. C. Peel, B. L. Finlayson, and T. A. McMahon, “Updated world map of the köppen-geiger climate classification,” *Hydrology and earth system sciences*, vol. 11, no. 5, pp. 1633–1644, 2007. doi: 10.5194/hess-11-1633-2007.

[61] M. Kottek, J. Grieser, C. Beck, B. Rudolf, and F. Rubel, “World map of the köppen-geiger climate classification updated,” *Meteorologische Zeitschrift*, vol. 15, pp. 259–263, 2006. doi: 10.1127/0941-2948/2006/0130.

[62] T. Wang, K. S. Lackner, and A. B. Wright, “Moisture-swing sorption for carbon dioxide capture from ambient air: A thermodynamic analysis,” *Physical Chemistry Chemical Physics*, vol. 15, no. 2, pp. 504–514, 2013. doi: 10.1039/c2cp43124f.

[63] D. X. Lan, *Noaa/gml trends*, Accessed: 2024-06-01, 2024. [Online]. Available: https://gml.noaa.gov/ccgg/trends/.

[64] Global Modeling and Assimilation Office, *MERRA-2 inst1_2d_asm_Nx: 2d,1-Hourly,Instantaneous,Single-Level,Assimilation,Single-Level Diagnostics V5.12.4*, Greenbelt, MD, USA, 2015. doi: 10.5067/3Z173KIE2TPD.

[65] D. M. Ruthven, *Principles of adsorption and adsorption processes*. John Wiley & Sons, 1984.

[66] D. Gunn, “Transfer of heat or mass to particles in fixed and fluidised beds,” *International Journal of Heat and Mass Transfer*, vol. 21, no. 4, pp. 467–476, 1978. doi: 10.1016/0017-9310(78)90080-7.

[67] C.-T. Tien, *Adsorption Calculations and Modeling* (Butterworth-Heinemann Series in Chemical Engineering). Butterworth-Heinemann, 1994.

[68] E. Glueckauf, “Theory of chromatography. part 10.—formulæ for diffusion into spheres and their application to chromatography,” *Transactions of the Faraday Society*, vol. 51, pp. 1540–1551, 1955. doi: 10.1039/TF9555101540.

[69] H. Schellevis, T. Van Schagen, and D. Brilman, “Process optimization of a fixed bed reactor system for direct air capture,” *International journal of greenhouse gas control*, vol. 110, p. 103 431, 2021. doi: 10.1016/j.ijggc.2021.103431.

[70] K. S. Hwang and W. K. Lee, “The adsorption and desorption breakthrough behavior of carbon monoxide and carbon dioxide on activated carbon. effect of total pressure and pressure-dependent mass transfer coefficients,” *Separation science and technology*, vol. 29, no. 14, pp. 1857–1891, 1994. doi: 10.1080/01496399408002177.

[71] C.-H. Lee, J. Yang, and H. Ahn, “Effects of carbon-to-zeolite ratio on layered bed h2 psa for coke oven gas,” *AIChE Journal*, vol. 45, no. 3, pp. 535–545, 1999.

[72] The Engineering ToolBox, *Universal and individual gas constants*, Accessed: 2024-06-01, 2024. [Online]. Available: https://www.engineeringtoolbox.com/individual-universal-gas-constant-d_588.html.

[73] The Engineering ToolBox, *Carbon dioxide - density and specific weight vs. temperature and pressure*, Accessed 21 March 2024, 2018. [Online]. Available: https://www.engineeringtoolbox.com/carbon-dioxide-density-specific-weight-temperature-pressure-d_2018.html.

[74] The Engineering ToolBox, *Molecular weight of substances*, Accessed: 2024-06-01, 2009. [Online]. Available: https://www.engineeringtoolbox.com/molecular-weight-gas-vapor-d_1156.html.

[75] M. Thirumaleshwar, *Fundamentals of heat and mass transfer*. Pearson Education India, 2006.

[76] The Engineering ToolBox, *Air - diffusion coefficients of gases in excess of air*, Accessed 21 March 2024, 2018. [Online]. Available: https://www.engineeringtoolbox.com/air-diffusion-coefficient-gas-mixture-temperature-d_2010.html.

[77] M. Tanaka, G. Girard, R. Davis, A. Peuto, and N. Bignell, “Recommended table for the density of water between 0 c and 40 c based on recent experimental reports,” *Metrologia*, vol. 38, no. 4, p. 301, 2001. doi: 10.1088/0026-1394/38/4/3.

[78] The Engineering Toolbox, *Air - density, specific weight and thermal expansion coefficient vs. temperature and pressure*, Accessed: 2024-06-01, 2024. [Online]. Available: https://www.engineeringtoolbox.com/air-density-specific-weight-d_600.html.

[79] Engineers Edge, *Viscosity of air, dynamic and kinematic*, Accessed: 2024-06-01, 2024. [Online]. Available: https://www.engineersedge.com/physics/viscosity_of_air_dynamic_and_kinematic_14483.htm.

[80] The Engineering ToolBox, *Atmospheric pressure vs. elevation above sea level*, Accessed: 2024-06-01, 2024. [Online]. Available: https://www.engineeringtoolbox.com/air-altitude-pressure-d_462.html.

[81] F. J. G. Ortiz, M. B. Rodríguez, and R. T. Yang, “Modeling of fixed-bed columns for gas physical adsorption,” *Chemical Engineering Journal*, vol. 378, p. 121 985, 2019. doi: 10.1016/j.cej.2019.121985.

[82] G. Towler and R. Sinnott, *Chemical engineering design: principles, practice and economics of plant and process design*. Butterworth-Heinemann, 2021. [Online]. Available: https://www.sciencedirect.com/science/book/9780128211793.

[83] M. S. Peters and K. D. Timmerhaus, *Plant design and economics for chemical engineers*. McGraw-Hill International, 1991.

[84] U.S. Bureau of Labor Statistics, *Cpi inflation calculator*, Accessed: 2024-06-09, 2024. [Online]. Available: https://www.bls.gov/data/inflation_calculator.htm.

[85] DuPont, *Amberlite fpa90 cl ion exchange resin data sheet*, Accessed: 2024-06-09, 2024. [Online]. Available: https://www.lenntech.com/Data-sheets/DuPont-Amberlite-FPA90-Cl-Ion-Exchange-Resin-L.pdf.

[86] DuPont, *Amberlite fpa90 cl, bulk*, Accessed: 2024-06-09, 2024. [Online]. Available: https://dws.octochemstore.com/product/amberlite-fpa90-cl/.

[87] Engineers Edge, *Density of common engineering materials*, https://www.engineersedge.com/materials/density_of_common_engineering_materials__15896.htm, Accessed: 2024-06-01.

[88] U.S. Bureau of Labor Statistics, *Inflation calculator*, https://www.bls.gov/data/inflation_calculator.htm, Accessed: 2024-06-01.

[89] DuPont DWS Online Store, *Amberlite fpa90 cl*, https://dws.octochemstore.com/product/amberlite-fpa90-cl/, Accessed: 2024-06-01.

[90] European Central Bank, *Currency converter*, https://data.ecb.europa.eu/currency-converter, Accessed: 2024-06-03.

[91] Ventilatieshop, *Ventilatieshop*, https://www.ventilatieshop.com/, Accessed: 2024-06-04.

[92] Holidu, *The water price index (eur)*, Accessed: 2024-06-09, 2021. [Online]. Available: https://www.holidu.com/magazine/water-price-index-intl.

[93] P. D'Odorico, D. D. Chiarelli, L. Rosa, A. Bini, D. Zilberman, and M. C. Rulli, "The global value of water in agriculture," *Proceedings of the national academy of sciences*, vol. 117, no. 36, pp. 21 985–21 993, 2020. doi: 10.1073/pnas.2005835117.

[94] European Central Bank, *Euro foreign exchange reference rates: Usd*, Accessed: 2024-06-09, 2024. [Online]. Available: https://www.ecb.europa.eu/stats/policy_and_exchange_rates/euro_reference_exchange_rates/html/eurofxref-graph-usd.en.html.

[95] GlobalPetrolPrices.com, *Electricity prices around the world*, Accessed: 2024-05-30, 2024. [Online]. Available: https://www.globalpetrolprices.com/electricity_prices/.

[96] M. Esmeijer, "Co2 in greenhouse horticulture," Applied plant Research, Tech. Rep., 1999.